Cavity Formation in Aluminum Irradiated with Aluminum Ions

Mark Lauren Sundquist

December 1974

UWFDM-101

Ph.D. thesis.

FUSION TECHNOLOGY INSTITUTE

UNIVERSITY OF WISCONSIN

MADISON WISCONSIN

Cavity Formation in Aluminum Irradiated with Aluminum Ions

Mark Lauren Sundquist

Fusion Technology Institute
University of Wisconsin
1500 Engineering Drive
Madison, WI 53706

http://fti.neep.wisc.edu

December 1974

UWFDM-101

Ph.D. thesis.

CAVITY FORMATION IN ALUMINUM IRRADIATED WITH ALUMINUM IONS

BY

MARK LAUREN SUNDQUIST

A thesis submitted in partial fulfillment of the requirements for the degree of

DOCTOR OF PHILOSOPHY

(Nuclear Engineering)

at the

University of Wisconsin

1974

CAVITY FORMATION IN ALUMINUM IRRADIATED WITH ALUMINUM IONS

Mark Lauren Sundquist

Under the supervision of Associate Professor John M. Donhowe

High-purity aluminum foil obtained from the same source as aluminum used in numerous fast-reactor irradiations[1] was irradiated in an experiment designed to show the effect of helium content on cavity formation.

Undoped samples irradiated between 50°C and 120°C and at doses up to 11 dpa produced only dislocation loops. Cavities and loops formed in samples preinjected with 0.1, 1 and 10 appm helium and irradiated at 100°C and 120°C to doses of about 2.3 dpa (5×10^{15} Al^{+}/cm^{2}). With irradiation at 75°C and below samples with 0.1 appm helium produced cavities and loops, but only loops formed in the 1 and 10 appm helium-implanted samples.

At 100°C the average cavity diameter and the cavity densities were not significantly different for the three helium levels, whereas at 120°C, the cavity size decreased with increasing helium content and the density increased.

The results indicate that a nucleating gas is probably required for the production of cavities in a pure metal. A combination of homogeneous and inhomogeneous nucleation is required to explain the variation in cavity formation with temperature.

Approved _____

[1]N.H. Packan, J. Nucl. Mat., 40, 1(1971) and
K. Farrell, A. Wolfenden and R.T. King, Rad. Effects, 8, 107(1971).

TABLE OF CONTENTS

FIGURES AND TABLES

Acknowledgements

The author would like to express his thanks for the continual advice and support given him by Professor J. M. Donhowe throughout the author's years in graduate school and for the many suggestions and ideas which made this experiment possible.

The author would also like to thank Dr. Michael Petrilak for an extensive introduction to the operation and care of the accelerator and its laboratory, Dr. Walter Yang for invaluable assistance with all aspects of the electron microscopy and sample preparation, and William Weber for calculations of helium-implantation energies and doses, for assistance with the implantation procedure and for working with the author throughout the long preparation of the experimental equipment.

The author has benefited from the advice and information on radiation-damage received from Professor G. L. Kulcinski, Professor R. A. Dodd and Professor F. J. Worzala.

The displacement density calculations were provided for the author by Halil Avci; Dr. A. Taylor of Argonne National Laboratory made many helpful suggestions on the operation of the heavy-ion source.

This work was supported by funds from the Atomic Energy Commission and the University of Wisconsin Graduate School.

I. Introduction.

The study of cavity formation in metals is motivated by the need to be able to predict the performance of materials subjected either to the fast neutrons produced by fast-breeder reactors or the combination of fast neutrons and energetic charged particles to be produced by future controlled-thermonuclear reactors. Two experimental systems exist for this study, irradiation in the available fast-neutron producing reactors and the simulation of fast-neutron irradiation by bombardment with charged particles. Fast-neutron irradiation is the logical means for the evaluation of possible reactor materials. The understanding of the basic mechanisms of cavity formation, however, requires isolation of variables such as temperature, dose and impurity content, which are difficult to separate in a reactor. This is especially true for the effect of helium since helium is produced by the (n,α) reactions in a fast reactor.

To observe the role of helium in cavity formation, an experimental system was developed which would irradiate a material with its own ions in a procedure designed to avoid contamination of the material with possible nucleating gases. Aluminum was chosen for the material because it is available in high-purity form and its melting point allows cavities to form at temperatures low enough to minimize contamination during irradiation. Furthermore, aluminum was known to be sensitive to irradiation and impurities; observable damage occurs at conveniently low doses and varies markedly with impurity type and concentration, as reported in previous experiments(13, 14, 17, 41, 16).

Even with the nearly ideal material, the simulation of neutron-

induced radiation with charged particles is subject to two problems. The procedure is more complicated than in reactor irradiation so there are more steps in which artifacts can be introduced. Secondly, the results depend on measurements made in the electron microscope; there can be no bulk measurements because the short ion range restricts the damage to a layer only a few microns thick. These difficulties can be overcome, however, and the observation of the effect of newly isolated variables is worth the experimental effort.

For the purposes of this thesis, the term cavity is used to mean a three-dimensional polyhedral opening in the lattice; both voids, which contain little or no gas, and bubbles, which contain gas in sufficient quantity to balance the surface tension of the lattice, are included in this term.

II. Previous Experiments

Observations of fast-neutron induced cavity formation occurred after the first experimental fast-breeder reactors were operated; they involved structural and cladding materials. Early studies on stainless steel included measurements made on EBR-II components retired after several years use (Claudson, et al., 1969 and Harkness and Li, 1969). The results of these experiments showed an approximately linear increase in total cavity volume, or swelling, with increased fluence. A second set of experiments in the EBR-II observed the effect of temperature (Harkness and Li, 1971). Cavities formed over the range from 375°C to 625°C with fluence from 2×10^{21} neutrons/cm^2 to 8.2×10^{21} neutrons/cm^2 (E> 0.1 Mev). The average cavity diameter increased with increased temperature, the number density decreased and the swelling reached a maximum between the temperature extremes. This has since been found to be typical behavior. It is discussed in the theory section.

Neutron-irradiation induced cavities in high-purity aluminum were first observed by Brimhall and Mastel (1969) in a sample which had been exposed to a fluence of 3.2×10^{19} neutrons/cm^2 (E> 1 Mev) at 50°C. Westmacott and Smallman (1970) carried out annealing studies and yield stress measurements on high-purity aluminum samples irradiated with a fluence of 1.6×10^{20} neutrons/cm^2 (E> 1 Mev). They found that radiation-induced cavities were eliminated only after long annealing times, implying that molecular hydrogen from the (n,p) reactions had stabilized the bubbles. The importance of hydrogen as a cavity-stabilizing gas is still not clear, however, since proton-irradiated samples studied with an Ion Microprobe Mass Analyzer showed no evidence of hydrogen entrap-

ment in the cavities (Keefer and Pard, 1973). In this experiment both stainless steel and tantalum samples were irradiated with 1.3×10^{19} to 7.4×10^{19} protons/cm^2 after being injected with 4.9 appm of helium. The importance of hydrogen may be questionable, but apparently some gas must be present.

The high-purity aluminum used on this thesis project was obtained from Dr. J.O. Stiegler at ORNL; it has been extensively studied under fast-neutron irradiation. Packan (1971) reported the variation in cavity size, density and swelling at 55°C after neutron fluences from 10^{19} to 10^{22} neutrons/cm^2 ($E > 0.82$ Mev). As fluence increased, the average cavity size increased, the cavity density increased, and the swelling increased. In another experiment with the same high-purity aluminum, Farrell, Wolfenden and King (1971) observed the change in cavity size and density as hydrogen and helium were added to the samples before irradiation with 4×10^{20} neutrons/cm^2 ($E > 1$ Mev). At 150°C the density increased strongly and the size dropped as gas content increased, but at 125°C the changes were not as clear. The results of both of these experiments will be discussed later in conjunction with the data from this thesis project.

The importance of non-gaseous impurities in the reduction of cavity density was shown by comparing the ORNL high-purity aluminum to commercial aluminum after irradiation with 3.5×10^{20} neutrons/cm^2 ($E > 0.82$ Mev). The high-purity samples contained numerous cavities, but the commercial material had only a few dislocation loops. Cubic cavities were formed in the commercial aluminum after a fast-neutron fluence of 1.5×10^{22} neutrons/cm^2 (Stiegler, et al., 1969).

The study of the microscopic effects of charged-particle irradiation on metals began earlier than fast-neutron studies, because particle accelerators were available to produce the necessary high-energy, high-density ion beams. Barnes and Mazey (1960) reported dislocation loops and vacancy clusters in copper and aluminum foils irradiated with α-particles from a cyclotron. Annealing experiments showed that the loops were formed by interstitials. The aluminum irradiation was repeated with 38 Mev α-particles (Mazey and Barnes, 1962), and diffraction contrast experiments confirmed the interstitial composition of the loops.

Cavities formed by 38 Mev α-particles were found in copper foils by Barnes and Mazey (1963). Studies on the migration and coalescence of those cavities led to the conclusion that the helium from the α-particles was relatively insoluble in the lattice and nearly all contained in the cavities. Later experiments with low-energy proton irradiation of copper revealed dislocation loops when irradiation took place within a certain temperature range (Mazey and Barnes, 1968).

Keefer, et al. (1970) reported the formation of cavities in 316 stainless steel irradiated with 1.2 Mev protons at 500°C. Radiation-induced dislocation loops and precipitate particles were also found.

A set of experiments bombarding 316 stainless steel with 100 kev hydrogen, carbon, oxygen and iron ions after varying concentrations of helium had been implanted in the targets investigated the need for gas atoms in the creation of cavities (Nelson and Mazey, 1969). Cavities were formed both with and without the injected helium, but in the case of iron and carbon bombardment the swelling increased markedly with helium concentration, in agreement with the neutron-irradiation experiments. The role of gas is not conclusively shown, however, since

stainless steel is such a complex system and the effect of any impurities is difficult to determine.

Attempts to simulate neutron damage by self-ion irradiation were carried out by Kulcinski, et al. (1970) by irradiating 316 stainless steel with 5 Mev copper ions. By calculating the total displacement density due to the copper bombardment at the depth of the electron microscope observation, it was possible to compare the cavity size and density to the results of fast-neutron irradiation done at the same total displacement density.

Since the initiation of the research for this thesis the results of another aluminum-ion irradiation of aluminum have been reported by Mazey, Francis and Hudson (1973). High-purity aluminum, implanted with 100 appm of helium, received doses of 3×10^{16} Al^{+}/cm^{2} and 6.25×10^{16} Al^{+}/cm^{2} at 400 kev, this corresponding to displacement densities of about 40 and 80 displacements per atom (dpa). This produced cavity densities of about 3.4×10^{16} cm^{-3} and 2.3×10^{16} cm^{-3} and average cavity radii of 50 A and 70 A, respectively.

This thesis work follows the fast-reactor work of Farrell, Wolfenden and King (1971) and Stiegler, et al. (1969) in observing the effect of gas concentration on cavity formation, but has the advantage of being able to show the result of irradiation in the complete absence of gaseous impurities. The techniques have evolved from those used in previous ion-bombardment work, and the radiation doses are given in terms of a displacement density as in Kulcinski, et al. (1970) and Mazey, et al. (1973) in order that some comparison can be made to the neutron irradiation of the same material.

III. Theory

Cavity formation requires the production of vacancies to a level above the equilibrium concentration,

$$C_v^e = A \exp\left(\frac{-E_{fv}}{kT}\right), \qquad (1)$$

where E_{fv} is the energy of vacancy formation, k is the Boltzmann constant and T is the absolute temperature. Vacancies are produced when lattice atoms are displaced during collisions with incident neutrons or charged particles. A displacement will occur if the energy transferred, T, is greater than E_d, the displacement energy, or when

$$T = \frac{4m_1m_2}{(m_1 + m_2)^2} E \sin^2\varphi/2 > E_d , \qquad (2)$$

where m_1 and m_2 are incident-particle and lattice-atom masses, E is the incident particle energy, and φ is the center of mass scattering angle.

Energetic neutrons and energetic ions can both produce displaced atoms having sufficient energy to generate a cascade of collisions and displacements. Since the number of displacements is generally far greater than the number of cascades, the majority of displacements in either neutron or ion irradiation is produced the same way, i.e., by collision with previously displaced lattice atoms. This simularity is the basic justification for ion-bombardment simulation of neutron-induced radiation damage.

There are, however, three main differences between ion-bombardment simulation and neutron irradiation; the first is that the displacements

in ion irradiation are produced in a thin layer near the surface of the target, whereas the mean free path of a neutron is generally much greater than the lengths of the individual cascades produced in the neutron's passing. Secondly, (n,α) and (n,p) reactions in fast-neutron irradiation produce helium and hydrogen during the irradiation, and as the effect of these gases is perhaps critical, they must be added during a simulation of neutron irradiation by ion bombardment. The third difference in the two irradiation systems is that in ion bombardment the bombarding ion always stays in the lattice; if this ion is not usually present in the material, then the simulation cannot be completely valid.

In ion bombardment the short ion range concentrates the damage, allowing much higher displacement densities to be produced than in neutron irradiation, but this also makes the observation of bulk property changes very difficult. On the other hand, ion bombardment is an ideal tool for the study of the role of solid or gaseous impurities since it is possible to isolate these impurities from the radiation dose, which is not possible in neutron irradiation.

In the self-ion irradiation in this research, the helium concentrations have been varied independently of the temperature and ion dose. The aluminum ions which initiated displacement cascades did not become impurities; they simply generated one extra interstitial per cascade. The effect of this is not precisely known, but it is thought to be negligible if the average number of displacements per cascade is more than about 1000 (Bullough and Perrin, 1971).

The displacement density is the parameter with which neutron irradiation data and ion bombardment simulation data can be compared. It is therefore important to be able to calculate this density.

Ions slowing down in metals lose energy by electron exitation and by nuclear collisions. The fraction of the incident energy lost to nuclear collisions can be found from the stopping power theory of Lindhard, Scharff and Schiøtt (1963). This value represents the fraction of energy delivered to displacements, but since each displacement produced will lose some of its energy by electron exitation, the total energy available for displacement production is considerably lower than the amount lost in nuclear collisions. This reduced nuclear energy loss divided by twice the energy needed to displace an atom gives the basic estimate of displacement density. It must be corrected with an efficiency term combining effects such as channeling and focusing and then adjusted for the straggling of the particle ranges. A program developed by Manning and Mueller (1973) has now become the standard displacement-density calculation; it is used for the displacement-density values in this thesis (Appendix B).

Cavity and Dislocation Loop Formation

Unlike displacement densities the densities of vacancies and interstitials in non-equilibrium situations cannot be calculated. It might be assumed that each displacement produces one vacancy and one interstitial, but the high mobility of these products allows loss by recombination and to sinks, making numerical estimates meaningless.

Cavity and loop formation depends on the vacancies combining to form small clusters, which will either grow into cavities or collapse into dislocation loops. The steady-state vacancy concentration can be discussed from a balance of production, which depends on displacement

density, and annihilation, either by vacancy-interstitial recombination or loss to vacancy sinks. The balance equation is

$$\alpha\nu = \beta D_i C_i C_v + \gamma_v p_s C_v D_v \quad , \tag{3}$$

where ν is the displacement density, α, β, and γ_v are constants, D_i and D_v are diffusion coefficients, and p_s is the vacancy sink concentration (Shewmon, 1971). The recombination term containing the vacancy diffusion coefficient has been dropped since the interstitial motion dominates the two terms. Since both diffusion coefficients increase exponentially with temperature, the vacancy concentration,

$$C_v = \frac{\alpha\nu}{\beta D_i C_i + \gamma_v p_s D_v} \quad , \tag{4}$$

should decrease with increasing temperature. At the temperature where the actual vacancy concentration approaches the equilibrium concentration (equation 1), the supersaturation necessary for cavity formation will no longer be present; this occurs at about half the melting point, T_{mp}, of most metals.

As the temperature is reduced the mobility of the vacancies decreases. The randomly produced divacancies and trivacancies are more likely to remain, thus decreasing temperature produces an increase in the number of potential cavities. The larger number of sites, however, coupled with the declining vacancy mobility causes the average cavity size to decrease with decreasing temperature. At about 0.3 T_{mp} cavity production stops entirely, because the very low vacancy mobility makes it more likely that a vacancy will meet a still active interstitial than another vacancy.

Continuing vacancy production at a temperature between 0.3 T_{mp} and 0.5 T_{mp} will cause these proto-clusters to grow. If a cluster takes the form of a dislocation loop, it will produce a strain field which will attract interstitials, thereby reducing the size of the vacancy cluster (Bullough and Perrin, 1971). If it grows into a three-dimensional cluster, Bullough and Perrin (1969) suggest that at some size it will collapse into a lower energy configuration. They base their argument on the stability of three simple defects, the spherical void of energy E_s, a plate-like void of energy E_p and radius r_p, and a circular dislocation loop of energy E_L and radius r_L. If the spherical void contains N vacancies, then

$$E_s = 4\pi\gamma \left(\frac{3\Lambda N}{4}\right)^{2/3} \quad , \tag{5}$$

where γ is the surface energy and Λ the vacancy volume. Similarly, the plate-like void has energy

$$E_p = \frac{2\gamma}{a_o}\Lambda N \quad , \tag{6}$$

where a_o is twice the (100) plane spacing. The loop has energy

$$E_L = \frac{2\pi\mu b^2}{5} \left(\frac{\Lambda N}{\pi a_o}\right)^{\frac{1}{2}} \quad , \tag{7}$$

where b is the Burger's vector of the loop, ($a_o/2$ $\langle 111 \rangle$), and μ is the shear modulus.

The plate-like void will collapse into the loop when $E_L < E_p$. This occurs in iron for $N \gtrsim 22$ vacancies. Similarly, the spherical void

will collapse when $E_L < E_s$; this occurs in iron only after $N \gtrsim 2140$ vacancies (Bullough and Perrin, 1969).

Bullough and Perrin (1969) use the energy model further to determine the behavior of voids and bubbles under conditions of mechanical stress and of vacancy supersaturation. The behavior of bubbles under compression is clearly different from that of voids; a bubble will shrink under hydrostatic pressure, whereas a void cannot maintain equilibrium and must collapse. Under tensile stress a bubble will expand in equilibrium until a critical radius is reached, then it will expand unstably. The void can be in equilibrium under tension but it must shrink to maintain equilibrium if the tension is increased; as this is unlikely, the normal fate of a void under tension is unstable growth. The pressure in a bubble is produced by the gas pressure and the surface tension; it is

$$P_B = \frac{L}{r^3} - \frac{2\gamma}{r} \quad , \tag{8}$$

where r is the bubble radius, and L is derived from the ideal gas law,

$$P = \frac{nkT}{V} = \frac{3}{4\pi r^3} nkT \quad ,$$

in the form

$$L = \frac{3}{4\pi} nkT \quad . \tag{9}$$

The pressure in a void has no gas contribution. It is defined only for negative pressures, i.e., tensile stress,

$$-P_v = -\frac{2\gamma}{r} \quad . \tag{10}$$

Equilibrium values for pressure and radius for bubbles and voids are shown in figure 1 (Bullough and Perrin, 1969).

Vacancy supersaturation produces a driving force favoring the migration of a vacancy to the surface of a bubble; Bullough and Perrin (1969) find it to be

$$F_s = \frac{kT}{b^3} \ln \frac{C_v}{C_v^e} \quad , \tag{11}$$

where b is the interatomic spacing. The driving force favoring the opposite migration under external compression is

$$F_m = P + \frac{2\gamma}{r} - \frac{3nkT}{4\pi r^3} \quad . \tag{12}$$

From this result, shown in figure 2, the behavior of voids and bubbles under different vacancy concentrations can be deduced; only voids of one radius can be in equilibrium at any given vacancy supersaturation, as given by equation (12) when n = 0,

$$r = \left(\frac{kT}{2\gamma b^3} \ln \frac{C_v}{C_v^e}\right)^{-1} \quad . \tag{13}$$

Voids larger than equilibrium size will grow, and voids smaller than equilibrium will shrink, leaving perhaps a few large voids.

Bubbles, however, are stable since they will grow or shrink in the direction of the equilibrium. The exception occurs when the bubble radius exceeds r_{crit}, in both figure 1 and figure 2, at which point unstable growth will occur.

From this discussion it seems clear that the stability of bubbles

FIGURE 1. Equilibrium Pressure vs. Bubble or Void Radius (Bullough and Perrin, 1969).

FIGURE 2. Non-Equilibrium Forces Tending to Expand or Shrink Bubbles and Voids (Bullough and Perrin, 1969).

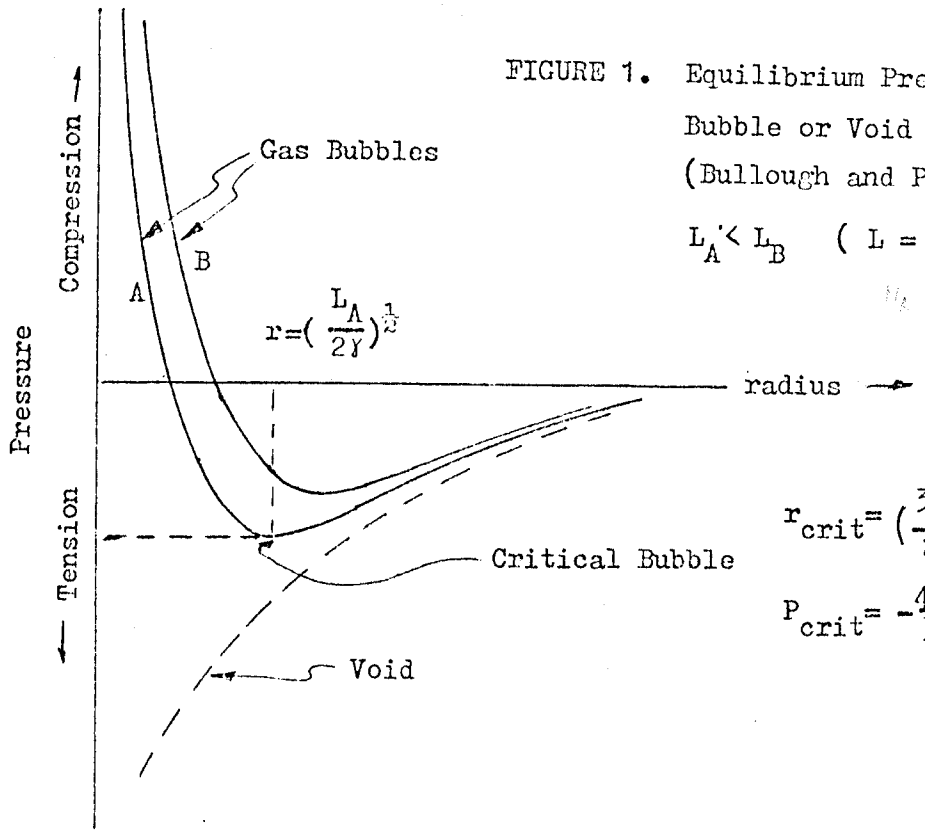

FIGURE 1. Equilibrium Pressure vs. Bubble or Void Radius (Bullough and Perrin, 1969)

$L_A < L_B$ ($L = \frac{3NkT}{4\pi}$)

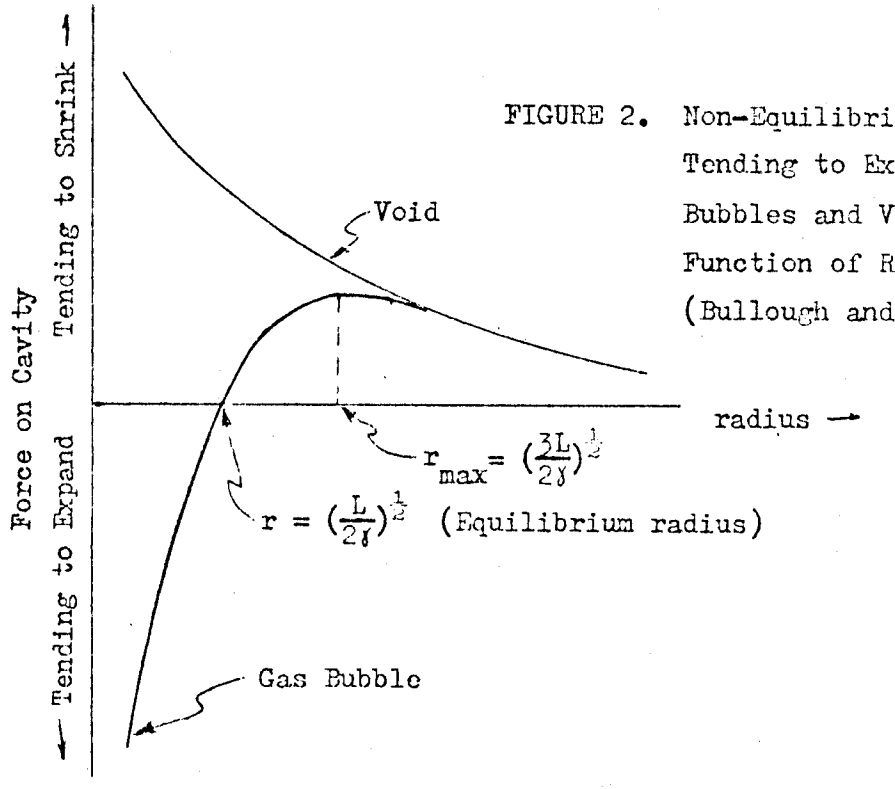

FIGURE 2. Non-Equilibrium Forces Tending to Expand or Shrink Bubbles and Voids as a Function of Radius (Bullough and Perrin, 1969)

over voids favors the existence of bubbles, and that irradiation in the absence of a nucleating gas should not be expected to form stable cavities.

It will, however, produce both interstitial and vacancy dislocation loops, but since the vacancy loops attract interstitials, perhaps only the interstitial loops will remain visible.

If a nucleating gas is present, then irradiation should produce cavities, and the cavity density should decrease with increasing temperature while the cavity size increases. As the gas content is increased, then more vacancy clusters should grow to become cavities, providing that there are sufficient vacancies available to make them all visible.

IV. Experimental Procedure

The observation of microscopic radiation damage depends on a reproducible and metallurgically correct sample handling procedure in which only one step, the irradiation, may introduce observable damage. The evolution of this procedure, along with the design and fabrication of the target chamber and the adaptation and installation of a heavy-ion source in the accelerator represent the main experimental activities of this thesis.

The experimental flow chart (figure 3) shows the sixteen steps and the equipment required for each. The high-purity aluminum foil was furnished by Dr. J.O. Stiegler of Oak Ridge National Laboratory in the form of annealed foils about 70 and 160 microns thick. The original analysis is in appendix A (Packan, 1971).

A. Preparation (Steps 1-6)

The procedure may be divided into three main parts: preparation (1-6), irradiation (7), and electron microscopy (8-16). The preparation steps differ for the pure and helium-implanted samples, whereas every other step must be the same. The helium injection was done with the Model 51 Electrostatic Generator in Sterling Hall. The irradiation system differed from the one described in step 7 only in that an electrostatic analyzer was installed between the accelerator and the magnetic analyzer and that an Ortec RF Ion Source was used to produce the helium ions. After the implanting was completed, the conversion of the accelerator to accommodate the Physicon Model 910 Heavy-Ion Source took place.

FIGURE 3. Experimental Procedure Flow Chart.
In addition to the equipment listed , each step may may require fine-tipped tweezers, acetone and methanol for handling and washing the samples.

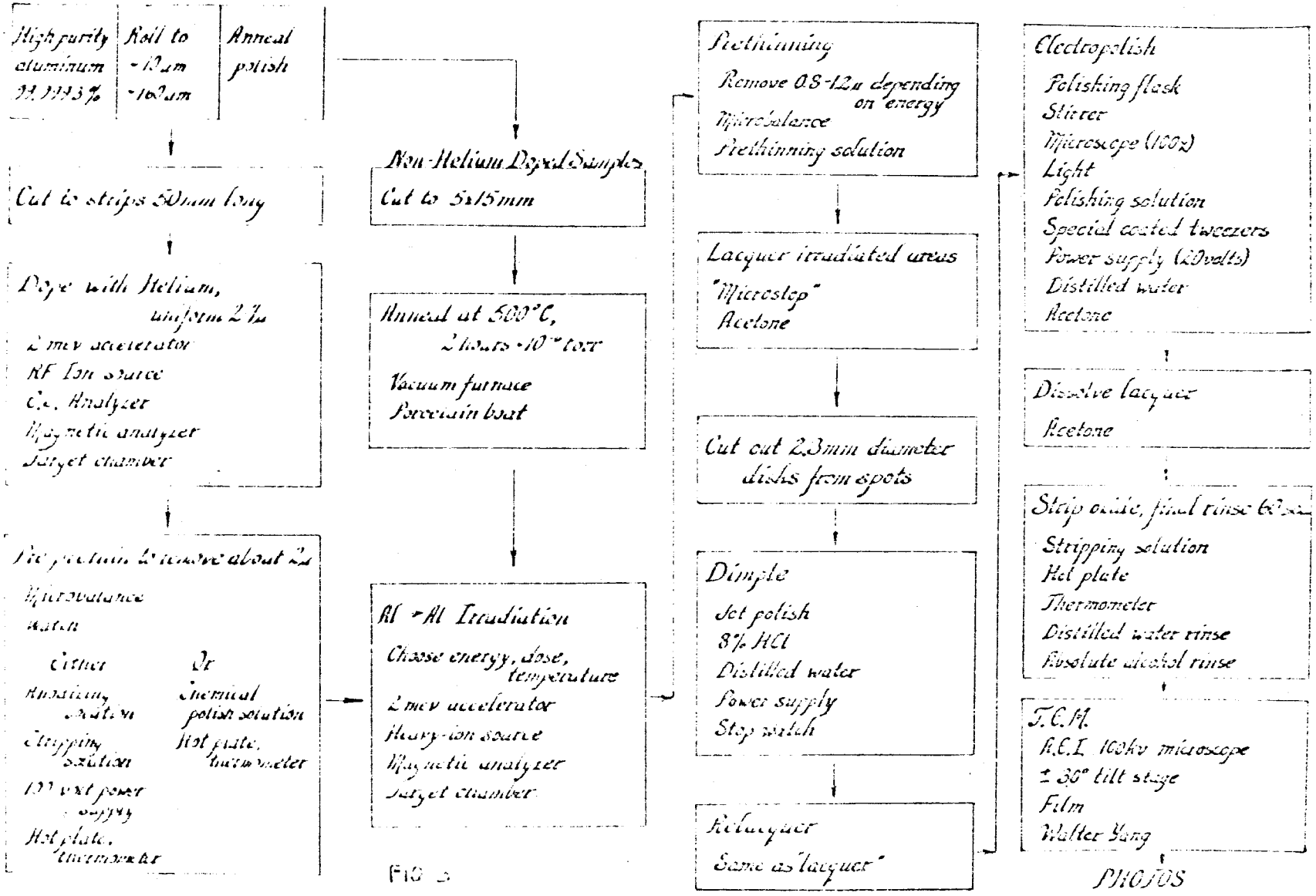
High purity aluminum 99.999%
Roll to ~10 μm ~100 μm
Anneal polish
Cut to strips 50mm long
Dope with Helium, uniform 2 μ
2 mev accelerator
RF Ion source
E. Analyzer
Magnetic analyzer
Target chamber
Die punch 2 remove about 2 μ
Microbalance
Water
Either
Ammonium sulfate
Stripping solution
100 volt power supply
Hot plate, thermometer
Or
Chemical polish solution
Hot plate, thermometer
Non-Helium Doped Samples
Cut to 5x15mm
Anneal at 500°C, 2 hours ~10⁻⁶ torr
Vacuum furnace
Porcelain boat
Al +Al Irradiation
Choose energy, dose, temperature
2 mev accelerator
Heavy-ion source
Magnetic analyzer
Target chamber
Fig 3
Electhinning
Remove 0.8-1.2 μ depending on energy
Microbalance
Electhinning solution
Lacquer irradiated areas
"Microstop"
Acetone
Cut out 2.3mm diameter disks from spots
Dimple
Jet polish
8% HCl
Distilled water
Power supply
Stop watch
Relacquer
Same as "lacquer"
Electropolish
Polishing flask
Stirrer
Microscope (100x)
Light
Polishing solution
Special coated tweezers
Power supply (20volts)
Distilled water
Acetone
Dissolve lacquer
Acetone
Strip oxide, final rinse 6%
Stripping solution
Hot plate
Thermometer
Distilled water rinse
Absolute alcohol rinse
T.E.M.
R.C.I. 100kv microscope
± 30° tilt stage
Film
Walter Yang
PHOTOS

During each room-temperature helium irradiation the beam energy was varied from 0.49 Mev to 1.98 Mev in 32 steps, each step matched to the estimated straggling of the helium ions in aluminum. The overall result was expected to be a uniform helium content from about 2 to 7 microns based on ranges given in Northcliffe and Schilling (1970) at levels of nominally 0.1, 1, and 10 appm. Immediately prior to aluminum-ion irradiation the depleted layer at the surface was removed either by chemical polishing or by an oxide-forming (anodizing)/oxide-stripping sequence developed by Mazey, et al. (1973). In both of these methods, used for this "pre-prethinning" step and also the prethinning (step 8), the sample strip was weighed, then thinned, weighed and thinned again until the desired amount was removed. The (anodizing/oxide-stripping) sequence was first used after electropolishing was rejected due to extreme non-uniformity of removal, and after RF sputter etching was tried and found to produce uniform removal over the sample strip, but irregular microsurfaces completely unsuitable for subsequent electron microscopy.

In the anodizing sequence an oxide layer was formed in an electrolytic solution of 30 grams of ammonium sulfate per liter of water. The oxide layer on the aluminum could then be removed by immersion in a stripping solution of 100g CrO_3, 100ml H_3PO_4 and 400 ml water at 90 to 100°C for one minute (Mazey, et al., 1973). If thin anodized layers were formed and stripped, the surface could be removed uniformly, and the removal monitored by weight loss. But perforations occurred in the very thin (70 micron) strips used for most of the helium-implanted samples, and consequently a chemical polishing method had to be tried. Samples to be chemically polished were immersed in a solution of 64% H_3PO_4, 18% H_2SO_4 and 18% HNO_3 at about 70°C. The removal was assumed to be

uniform, as the surface polished uniformly, and no perforation or pitting occurred. Since the chemical thinning was evidently just as uniform as the sometimes troublesome anodizing process, and since it also improved the microscopic smoothness of the surface, it replaced the anodizing sequence for the latter part of the experiment. Control samples taken through the procedure without aluminum-ion irradiation showed no sign of radiation damage from the helium injection, and the low dislocation density reflected the care taken to avoid mechanical deformation in any step.

B. Aluminum-Ion Irradiation (Step 7)

The irradiation step requires a source of aluminum ions, the accelerator and beam-handling equipment (figure 4), and a target chamber. The target chamber (figure 5) consists of an all-metal vacuum system capable of routine operation in the 10^{-9} torr vacuum range. A sylphon bellows allows the target holder to move over a 5 cm range; a straight-through valve can isolate the system from the accelerator, and the beam can be viewed on a quartz disk in the window opposite the beam entry port.

Two of the interchangeable target holders are designed for high-temperature irradiation; one is made of stainless steel, usable between 150°C and 700°C, and the other, usable up to 1100°C, is made of molybdenum and a tungsten-tantalum alloy. Both are heated by electrons from a negatively-biased filament. The target holder for aluminum samples (figure 6) utilizes a 20-watt thermo-electric module to heat or cool the sample between room temperature and 120°C. A 30 cubic inch aluminum bar acts as a heat sink for the module. Temperature is measured on a thermocouple meter accurate to $\pm$ 1°C; the thermocouples on the front mask also

collect the beam current hitting the electrically isolated sample. Since the beam power in these experiments rarely exceeds 20 mw, the thermocouple-to-sample intimacy is not considered to be critical, and the overall temperature accuracy should be within $\pm$ 2°C.

The 2 Mev Model 51 Electrostatic Generator was converted to a heavy-ion accelerator with the installation of a Physicon Model 910 Ion Source. The adaptation required a complete rebuilding of the accelerator high-voltage terminal, including new ion-source power supplies and telemetry, the design, installation and adjustment of a new electrostatic lens to couple the source to the accelerating tube, and the installation of a 2 kw, 400 Hz three-phase alternator to power the source supplies. The source housing was rebuilt to eliminate numerous "O"-ring seals, and a 4-inch diffusion pump, liquid-nitrogen cold trap and gate valve were installed on the accelerator beam tube, and a liquid-freon circulatory system was built to cool the source.

The ion source (figure 7) consists of a cylindrical graphite ionization chamber containing a 1 mm thick tungsten filament, a solenoidal magnet to produce an axial field in the chamber, and a quartz tube containing aluminum powder in a position where it will be heated during source operation. Energizing the filament also turns on a heater on the CCl_4 bottle, and the vapor generated passes over the aluminum powder at end of the ionization chamber. According to Sidenius and Skilbreid (1961) the following reactions take place:

$$Al_2O_3 + CCl_4 \rightleftharpoons 2AlOCl + COCl_2 \qquad (14)$$

$$AlOCl + CCl_4 \longrightarrow AlCl_3 + COCl_2 \qquad (15)$$

The aluminum chloride and the phosgene will pass into the ionization chamber where they will be broken up and ionized. When the source is properly adjusted for aluminum-ion production, the anode voltage is too low for optimum production of gases such as nitrogen and oxygen.

The aluminum, carbon and chlorine ions produced by the source, along with small numbers of oxygen and possibly nitrogen ions, are extracted and focused by a three-element electrostatic lens and then travel through the accelerating tube, past vertical and horizontal deflection plates, to the entrance of the magnetic analyzer.

The magnetic analyzer separates the components of the beam by mass, according to the formula,

$$BR = \left(\frac{2mV}{e}\right)^{\frac{1}{2}} , \qquad (16)$$

where B is the magnetic field, R is the effective radius of curvature of the analyzer, V is the accelerating potential, m the particle mass and e the electronic charge. This assumes that the source products are singly ionized; the effective radius of curvature is obtained from calibration with known masses. The accelerator can be stabilized automatically by taking an error signal for the energy-control feedback loop from a slit assembly between the magnet and the target. The dispersion of the 15° sector magnet at mass 27 is about 0.25 degrees per amu; this separates the aluminum component from any possible nitrogen beam by over three times the width of the opening in the sample mask, assuring a pure aluminum beam at the target. Further guarantee of this purity is in the inability of the ion source to produce a significant nitrogen component when the source is optimized for aluminum production.

A typical irradiation required several hours to warm up and equilibrate the ion source and one to two hours of irradiation for a dose of one displacement per atom (dpa). Samples were moved into the beam only when they had reached the run temperature, and when the magnetic analyzer was adjusted to allow only the aluminum component of the beam to hit the target. The beam current hitting the sample was measured with an electrometer and integrated with respect to time until the desired dose was reached. Then the target holder was moved vertically with the sylphon bellows until the beam hit the next sample. Several samples were usually irradiated in sequence after the source was warmed up, but always in order of decreasing temperature. At worst a sample already irradiated at 120°C would remain at 120°C for less than two hours while a second sample was irradiated; samples were never raised to higher temperatures after irradiation except in the relatively rapid chemical polishing steps (70°C for 30 seconds) or oxide stripping steps (90°C for several minutes). None of this should have affected the cavity formation since previous annealing studies done at ORNL on the same high-purity foil showed no reduction of swelling below 150°C and no disappearance of smaller defects until 200°C, with full damage removal requiring 20 hours at 237°C (Jostsons, Long, Stiegler, Farrell and Braski, 1971, and Packan, 1971).

C. Electron Microscopy Preparation (Steps 8-16)

The purpose of the "pre-prethinning" step for the helium implanted samples was to remove the layer not injected with helium; the prethinning step used the same method, but it was done in order to observe the damage at a depth on the displacement-density curve which gives the desired dpa

value (appendix B). The values nearer to the peak of the curve have a greater probable error than the values near the surface for a given error in depth measurement since the curves are steeper near the peak. However, as even the steepest part of the curve gives only a $\pm$ 10% error in dpa for a $\pm$ 5% error in depth, and because the repeatability of the thickness measurements was considerably better than $\pm$ 1%, no limitations were placed on energy or depth choices. The error in depth observed depends more on the uniformity of the thinning process and to some extent on the final thickness of the transparent layer bordering the thinned surface than on the far greater accuracy of the weighing measurements. As these two effects are difficult to measure, the reproducibility of the results must reflect back on the assumption of uniform removal.

Steps 9 through 15 are variations of standard electron-microscopy preparation with the added difficulty that no more material may be removed from the irradiated and prethinned side. The jet-polished dimple confines the final perforation to the center of the irradiated spot, and the laquer prevents further removal or polishing of the irradiated side during the final electropolishing step. Consequently the polish before irradiation must be of sufficient quality to produce usable transparent areas. Control samples verify that the cutting out of the samples with a deftly-handled razor blade or scalpel produced virtually no mechanical deformation in the irradiated zone.

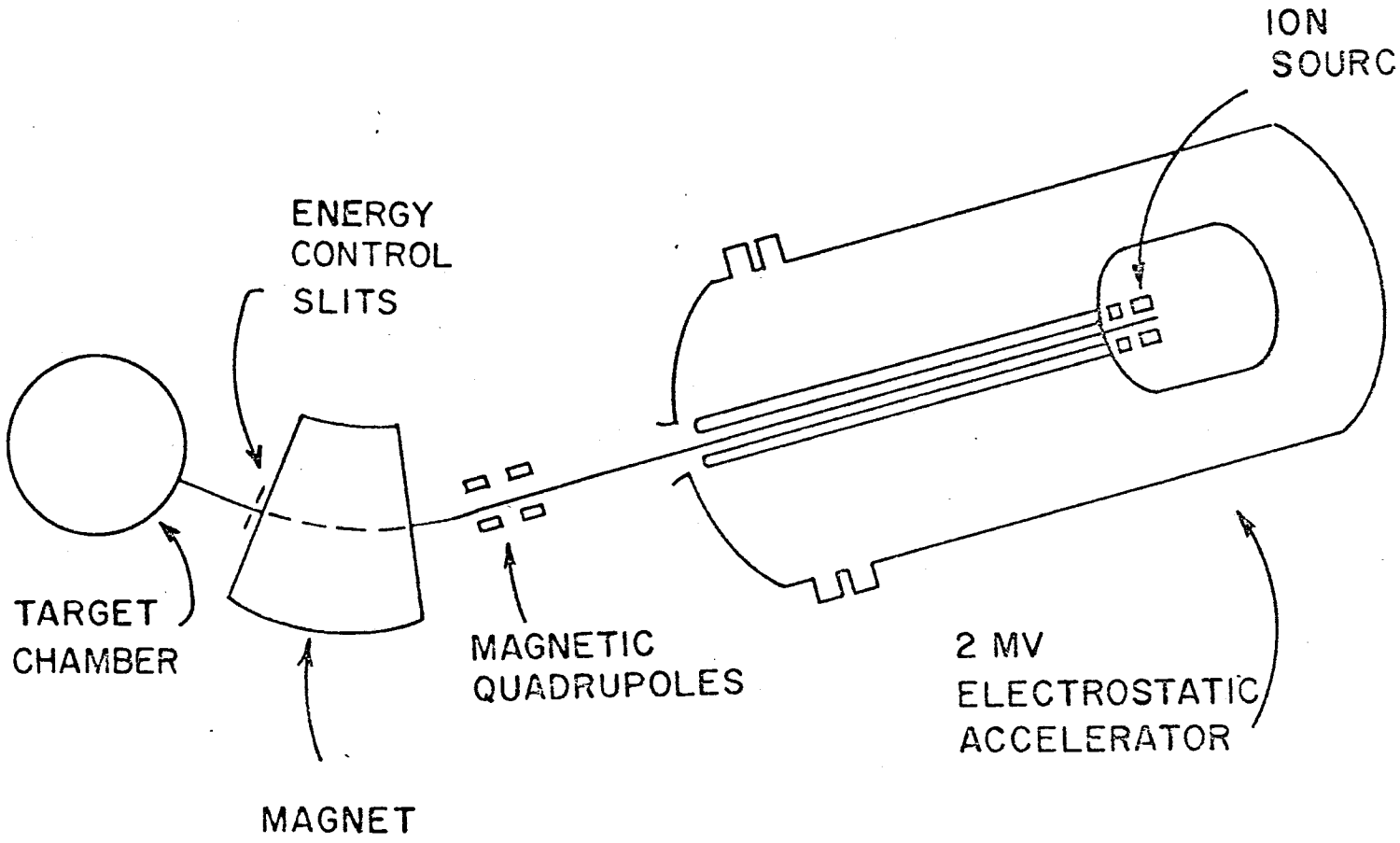

FIGURE 4. IRRADIATION SYSTEM SCHEMATIC

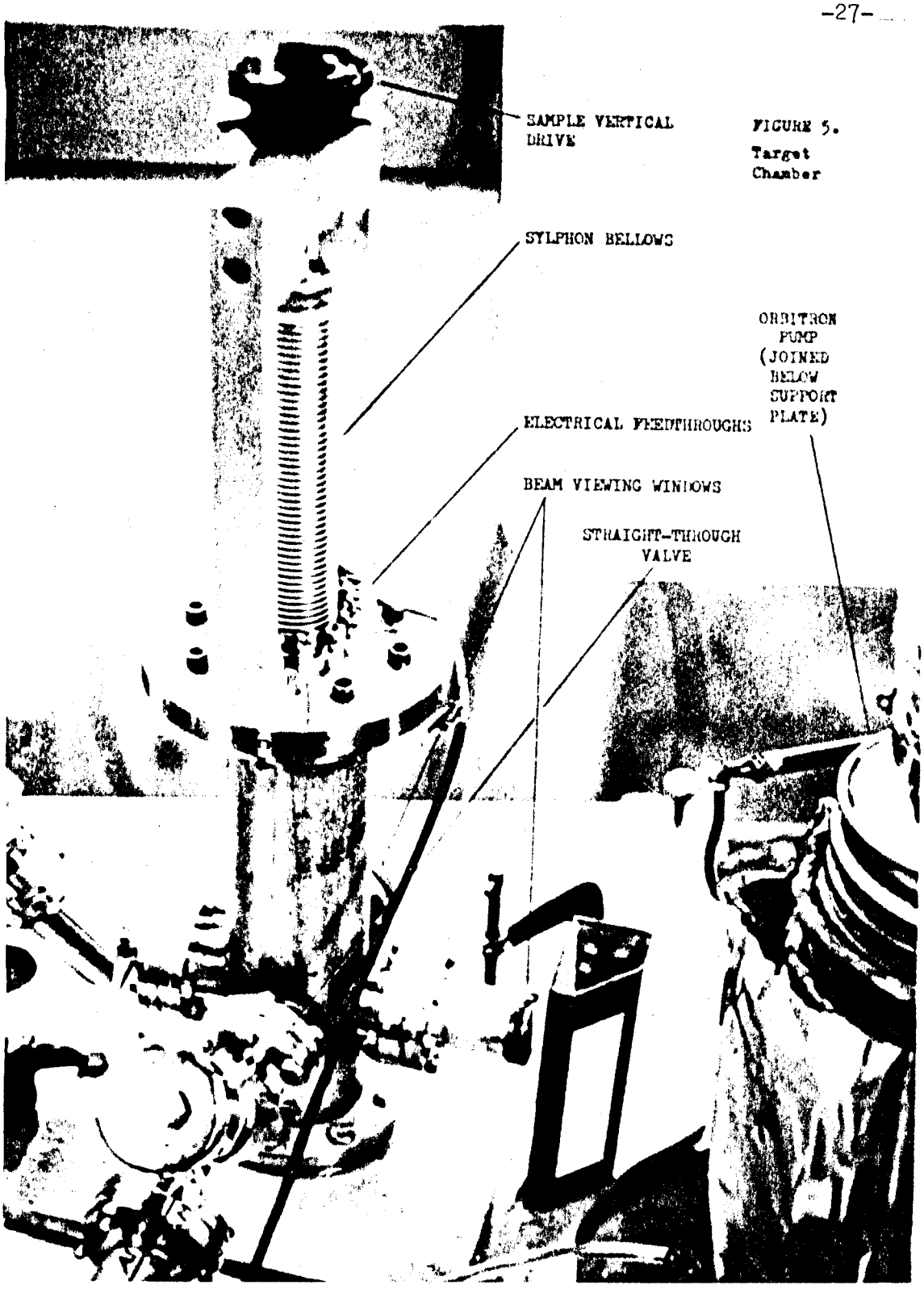

FIGURE 5.
Target Chamber

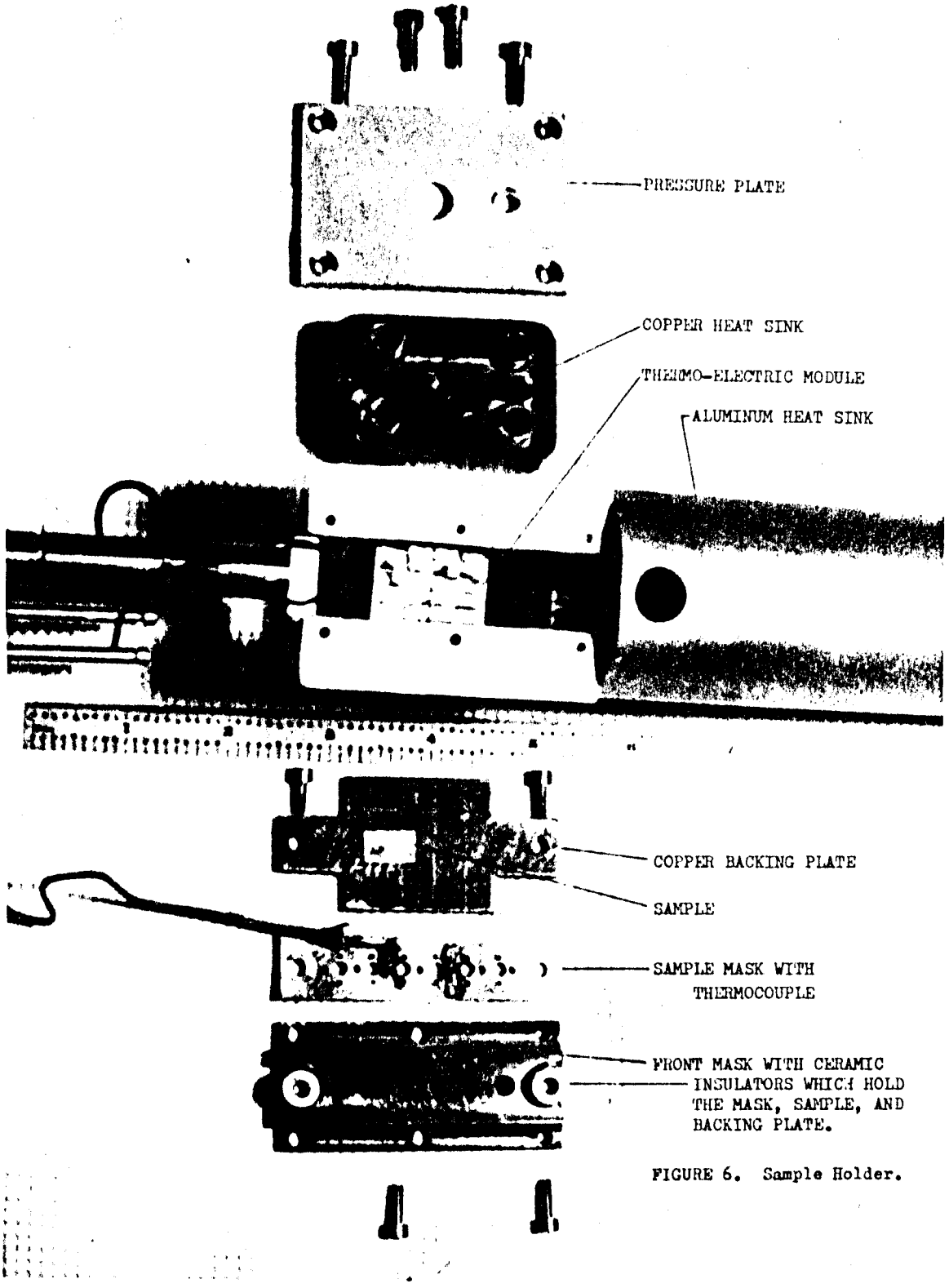

FIGURE 6. Sample Holder.

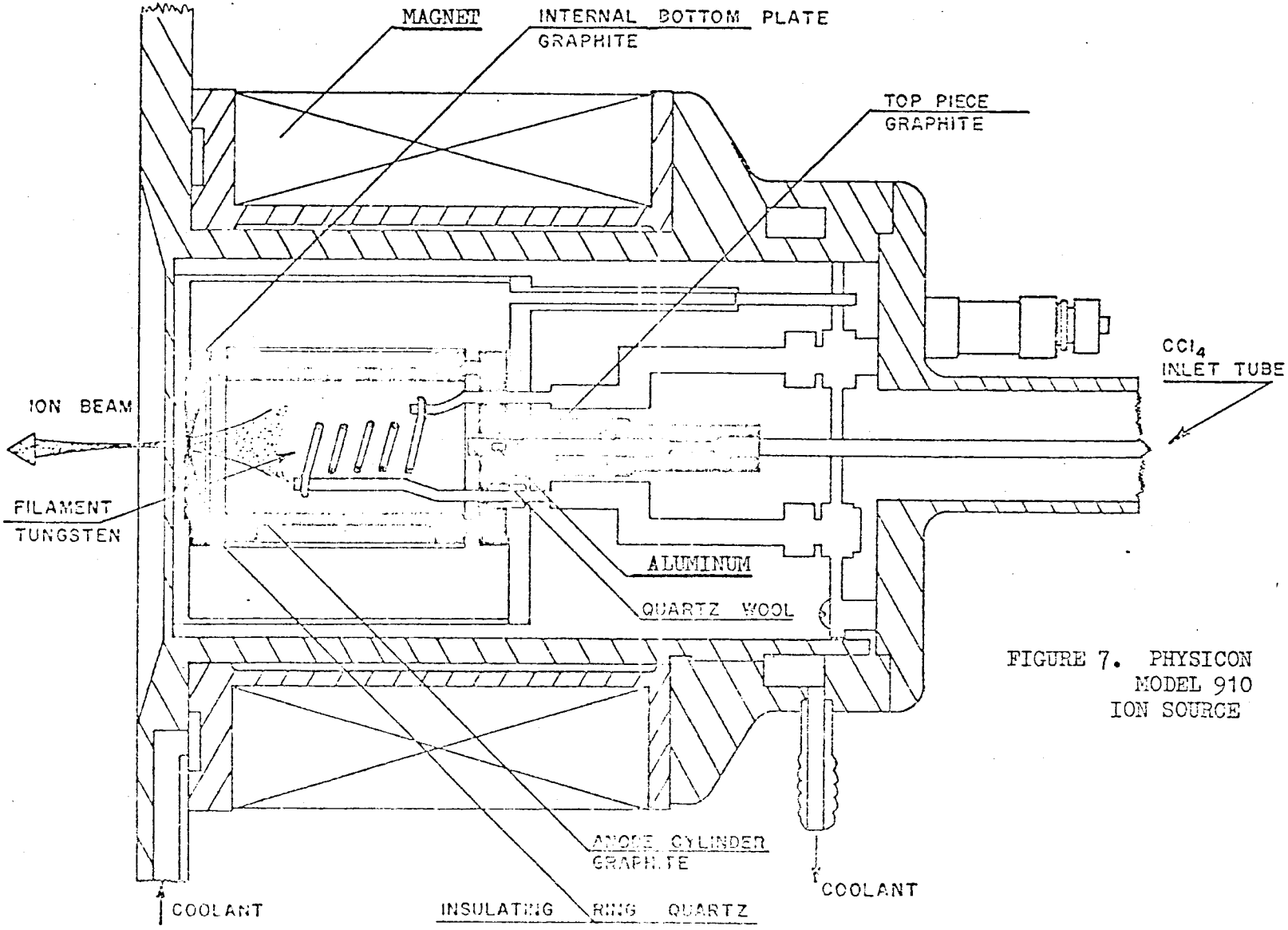

FIGURE 7. PHYSICON MODEL 910 ION SOURCE

V. Experimental Results

Between November 1973 and February 1974, over thirty samples of low-purity aluminum were irradiated. A few were prepared for the electron microscope, but they mainly served as practice samples with which the new ion-source behavior could be learned. After the irradiation system became predictable, seventeen high-purity samples were irradiated from February 1974 to the end of April. The first eight were lost through unsuccessful prethinning by electropolishing or RF sputter etching. Then the anodizing/stripping technique (Mazey, et al., 1973) was used and dislocation loops were found in the rest of the pure samples. The last sample in the series was irradiated to a dose of eleven dpa, and still no cavities were formed.

The successful prethinning technique was used for removing the two-micron depleted layer on the helium-implanted samples; cavities were found in the first sample, run under the same conditions as the pure samples. The procedure was finally complete, and twenty-eight of the remaining thirty-two helium-doped samples were prepared and irradiated in the matrix shown in figure 8. The only subsequent change in procedure was the use of the chemical thinning technique; its introduction did nothing but reduce the polishing loss rate from over 20% to less than 16% and simultaneously improve the quality of the thin areas seen in the electron microscope.

A. Qualitative Results

Figure 8 shows the qualitative results. Cavities formed only in

Helium Level ↓ \ Temperature, °C	30	50	75	100	120
10 appm			A-0-10-36 LOOPS	A-0-10-18 A-0-10-19(L) CAVITIES	A-0-10-20 A-0-10-21(L) A-0-10-22 CAVITIES
1 appm	A-0-01-40 A-0-01-41 LOOPS	A-0-01-31 A-0-01-32 A-0-01-39 LOOPS	A-0-01-29 A-0-01-30 A-0-01-37 A-0-01-38(L) LOOPS	A-0-01-25(L) A-0-01-26 CAVITIES	A-0-01-27 A-0-01-28 CAVITIES
0.1 appm		A-0-X1-46 A-0-X1-47 CAVITIES	A-0-X1-44 A-0-X1-45 CAVITIES	A-0-X1-23 A-0-X1-24 A-0-X1-33(L) A-0-X1-34 CAVITIES	A-0-X1-42 A-0-X1-43 CAVITIES
No Helium	NP = Not Polished L = Bad Polish	A-0-00-15 A-0-00-16(NP) LOOPS	A-0-00-11 A-0-00-12(NP) LOOPS	A-0-00-7(L) A-0-00-8 A-0-00-9(L) A-0-00-10(NP) A-0-00-17 LOOPS	A-0-00-13 A-0-00-14(NP) LOOPS

FIGURE 8. Qualitative Results.

the helium-implanted samples; at the higher two helium levels cavities formed only at the two higher temperatures. The need for a nucleating gas is strongly suggested by the theory of Bullough and Perrin (1969, 1971) and strongly supported by these results. Even at displacement densities about five times higher than used in the helium-implanted samples, the pure samples would not produce cavities.

At lower temperatures theory suggests that there will be more proto-clusters formed; if more helium is present, more of these clusters will be nucleated and a larger number of clusters will compete for the available vacancies. The result is that more irradiation is needed to produce visible cavities. The rise in the threshold for cavity formation can be estimated from the variation in cavity density with temperatures in the 0.1 appm helium-implanted samples. This will be discussed with the quantitative results.

A grain boundary was visible in one sample, and a distinct line of cavities ran parallel to this boundary at a distance of about 2000 Å (see insert on figure 12c). This was due to the ability of the grain boundary to act as a sink for the vacancies and interstitials formed near it, eliminating the vacancy supersaturation needed to produce cavities.

Dislocation loops were usually found in the same areas as cavities, but they require a particular crystal orientation in the electron microscope to have contrast (figure 11a). Cavities are visible at any angle, and for clarity most pictures were taken without the loops in contrast.

The cavities were octahedral with faces of (111) planes. Figure 15 shows three different views of the cavities, with the octahedra

projected as hexagons (111), squares (001) and diamonds (110). Face-centered-cubic materials generally produce octahedral cavities; aluminum under neutron irradiation produces exactly the same cavity shapes (Packon, 1971).

Elongated cavities were seen in one sample irradiated at 100°C and containing 0.1 appm helium. They were similar to the elongated cavities found by Farrell, Wolfenden and King (1971), but as only two of them were seen, no conclusions could be drawn.

Figures 11, 12, and 13 show the variation in cavity size and density with temperature at each level of helium and figure 14 shows the variation in cavity formation as a function of helium level at 100°C. The lower temperatures at 1 and 10 appm helium only produced dislocation loops, as did the samples without helium (figure 14a).

B. Quantitative Methods

Electron-microscope photographs provided quantitative measurements of the size and density of the cavities. Size measurements were made from enlarged prints using a Zeiss Particle Size Counter. A light spot from this instrument can be focused to match the size of a cavity on a negative or print; adjusting the light spot automatically connects a switch to one of forty solenoid-operated counters. When the spot size matches the cavity, a second switch is closed, sending power to the counter corresponding to the spot size, and a needle perforates the cavity on the photograph. The pin prick makes it easy to avoid counting any cavity more than once and a size histogram is automatically recorded. Matching a circular spot to the various projections of the

octahedra seen in the photographs was done by trying to equalize the area of the spot with the area of the projection. The possible systematic error in this method was judged to be small compared to the statistical variations in the cavity size and to the random errors in matching caused by the lack of distinct cavity boundaries in some photographs. In the data tabulation and text cavity size will henceforth refer to average cavity diameter.

Density measurements require an estimate of foil thickness. If a sample showing a field of cavities is tilted a known amount, θ°, symmetrically about a known axis and photographs taken at $\pm\theta$, the resultant parallax is proportional to the depth difference of the cavities in the photographs. If the difference in the distance from the tilt axis in a pair of cavities varies from one of the stereo photographs to the other, then the height difference is

$$\Delta z = \frac{\Delta x}{2M \sin\theta} \quad . \qquad (17)$$

For example, in a photograph taken at -5° tilt the distance between two cavities measured along a line perpendicular to the tilt axis is 0.45 cm; on the $+5^{\circ}$ tilt photograph the same two cavities differ only 0.11 cm in their distances to the tilt axis. This makes the parallax 0.45 - 0.11 = 0.34 cm, and the height difference is then

$$\Delta z = \frac{\Delta x}{2M \sin\theta} = \frac{0.34 \text{ cm}}{2(126000x) \sin 5^{\circ}} = 1550 \text{ A} \quad .$$

If a stereo pair is scanned visually to choose pairs if highest and lowest cavities, the parallax of these pairs can be measured; the foil

thickness will be slightly greater than the height difference of those cavities. In several of the foils observed the transparent areas were too small and irregular to warrant stereo micrographs; in several other cases the goniometer on the electron microscope failed to operate properly. The thickness reported for these samples is an estimate based on the measured thickness of other samples, but statistical variations expected with the small number of cavities visible in the poor samples should overshadow the error in the thickness estimate.

The aluminum-ion doses for most of the samples were the same, but as the energy was varied, the depth of prethinning was chosen so that all the samples would have about 2.3 dpa, according to the displacement-density curves in appendix B. The actual dpa values ranged from 1.85 dpa to 2.75 dpa, because the prethinning was not always stopped at the correct thickness. It was necessary to normalize the density, average size and density results slightly to correct this discrepancy. This was done by correcting the cavity size by dose to the 0.2 power and density by dose to the 0.6 power, or

$$(\text{Cavity size}) \propto (\text{Dose})^{0.2}$$

$$(\text{Cavity density}) \propto (\text{Dose})^{0.6}$$

This results in swelling increasing as dose to the 1.2 power, in approximate agreement with the dose dependency of neutron-irradiated aluminum (Packan,1971). Considering the small corrections to be made here, the normalization should improve the results. The sample irradiation data, dpa levels and raw density and size data are shown in Table I, along with the normalized density, size and swelling data also plotted

Sample	E	Dose	Time	Temp	Depth	DPA	Thick-ness	n	%	Density °C	Density N	Size	±	Diam	ΔV/V
A-0-10-18	1.2	5.3	125	100	A/S 0.95	1.94	1600	68	12	3×10^{14}	3.3×10^{14}	306	52	317	.55
A-0-10-20	1.2	5.3	111	120	A/S 0.92	1.85	(2000)			(3×10^{15})	(3.4×10^{15})	160	49	167	(.83)
A-0-10-22	1.2	11.0	260	120	A/S 1.13	4.32	1900	84	11	1.1×10^{15}		308	85		
A-0-X1-23	1.4	5.3	121	100	A/S 1.07	1.82	1000	21	22	3×10^{14}	3.5×10^{14}	304	55	318	.59
A-0-X1-24	1.4	5.3	101	100	A/S 1.07	1.82	(1000)	21	22	(9×10^{13})	(1×10^{14})	307	103	322	(.17)
A-0-01-26	1.4	5.3	114	100	A/S 1.18	2.27	(1500)	26	20	(1.3×10^{14})	(1.3×10^{14})	253	82	255	(.11)
A-0-01-27	1.4	5.3	101	120	C 1.18	2.27	(1500)	5	50	(6×10^{13})	(6×10^{13})	410	128	411	(.22)
A-0-01-28	1.4	5.3	116	120	C 1.18	2.27	ID	1							
A-0-X1-34	1.4	5.3	156	100	C 1.30	2.51	ID								
A-0-X1-42	1.2	5.3	72	120	C 1.17	2.75	(1500)			(1.5×10^{14})	(1.3×10^{14})	462	130	446	(.60)
A-0-X1-43	1.2	5.3	73	120	C 1.17	2.75	1600	12	29	1.2×10^{14}	1.1×10^{14}	491	130	474	.61
A-0-X1-45	1.2	5.3	74	75	C 1.04	2.42	1400	183	7	2.1×10^{15}	2×10^{15}	184	50	182	.63
A-0-X1-46	1.2	5.3	66	50	C 1.04	2.42	600	162	8	4×10^{15}	4×10^{15}	143	45	142	.58
A-0-X1-47	1.2	5.8	65	50	C 1.04	2.63	1000	36	17	1.2×10^{15}	1.1×10^{15}	153	28	149	.19

Second number is Helium content.

Mev.

Al^{+}/cm^{2}.

Minutes.

Degrees C.

Depth-microns. A/S = Anodize/Strip. C = Chemical Polish.

Appendix B.

(-) = Estimates. ID = Data Insufficient.

$n^{\frac{1}{2}}/n \times 100$. Number of cavities

$Cavities/cm^{3}$.

$Cavities/cm^{3}$ normalized to 2.30 DPA.

Average Cavity Diameter, Å.

Standard deviation, Å.

Normalized to 2.3 DPA, in Å.

% Swelling.

TABLE I. Data from Samples Containing Cavities

in figures 9 and 10.

The error bars for the cavity size points are the standard deviations of the cavity size distributions observed with the Zeiss Particle Size Counter. This assumes a Gaussian distribution. The probable statistical error in the density measurements in Table I reflects the number of cavities contributing to a measurement. The systematic errors in the density and size measurements will be discussed later.

C. Variation with Temperature

The temperature variation of cavity size and density in the samples implanted with 0.1 appm helium and 1 appm helium agrees with the results of experiments on other materials. At these helium levels the decreasing cavity density and increasing cavity size with increasing temperature support the model of "homogeneous nucleation" discussed in the theory section. The two samples containing 10 appm helium did not fit this model, however, as the size and density changes were in the opposite direction. It is interesting to note that this behavior also occurred in high-purity aluminum from the same source as that used in this thesis when the material was irradiated with 4×10^{20} neutrons/cm^2 ($E > 1$ Mev) by Farrell, Wolfenden and King (1971). Table II shows the reversal occurring in both sets of data.

TABLE II (See also figure 9).

	125°C (Farrell, et al.)			150°C	
Uninjected	2.8×10^{13}	70 Å	density down, size up →	1.2×10^{12}	170 Å
3 appm helium	1.4×10^{13}	80 Å	density up →	2.6×10^{13}	70 Å
	100°C (This thesis)			**120°C**	
0.1 appm helium	3.5×10^{14}	320 Å	density down, size up →	1.1×10^{14}	460 Å
1 appm helium	1.3×10^{14}	260 Å		6×10^{13}	410 Å
10 appm helium	3.3×10^{14}	320 Å	density up, size down →	3.4×10^{15}	170 Å

In the uninjected neutron-irradiated aluminum of Farrell, Wolfenden and King, the temperature increase reduced the density and increased the average cavity size, but the aluminum with 3 appm helium showed the reverse, a reduction in size and an increase in density. The same reversal takes place in the ion-bombarded samples.

It is difficult to explain this behavior without data at lower temperatures. In the ion bombardment no visible cavities formed at 75°C or lower when the helium content was 1 or 10 appm, suggesting that the density of nucleated clusters was perhaps to high for any of them to grow to visibility. This tends to support the homogeneous nucleation model, but is not entirely convincing, because the densities at 1 appm are already lower than those at 0.1 appm and the same rise would be expected in both the 1 and 0.1 appm cases. It is possible, however, that the measured densities at 1 appm are low due to the presence of a grain boundary in the 100°C sample; Farrell, Wolfenden and King (1971) report somewhat lower densities near grain boundaries. Raising the 1 appm density would decrease the slope of the density curve (figure 9, lower) and suggest higher densities than in the 0.1 appm case at lower temperatures. Then it could be argued that there were insufficient vacancies to allow

any of the nucleated cavities to grow to visible size. Clearly it will be useful to establish the threshold values for both the 1 and 10 appm helium-implanted samples at the lower temperatures.

It is possible that an increase in the dose would result in "normal" temperature variations similar to the 0.1 appm helium-doped samples, that the 10 appm ion-bombarded samples and the 3 appm neutron-irradiated samples simply have far more helium than their doses can make use of. Mazey, et al.(1973) reported on two samples of high-purity aluminum containing 100 appm helium, irradiated with 400 kev aluminum ions at 40 and 80 dpa and at 50°C and 75°C (Table III). Even though the 75°C sample has twice the dose of the 50°C sample, its cavity density is lower. Applying the normalization used earlier, the rise in cavity size from the 50°C sample is seen to exceed the increase in size expected from dose alone. This implies that the temperature effect is dominant here, and that these 100 appm samples exhibit "normal" behavior at 40 dpa.

TABLE III (Mazey, et al., 1973)

		As reported		Normalized to 40 dpa	
50°C	40 dpa	3.4×10^{16}	100 Å	3×10^{16}	100 Å
75°C	80 dpa	2.3×10^{16}	140 Å	1.5×10^{16}	114 Å

From this it is estimated that about 10 dpa would probably produce cavities at 1 appm helium below 100°C, and that about 20 to 30 dpa would be needed at 10 appm to produce "normal" behavior.

FIGURE 9. Average Cavity Diameter vs. Temperature and Cavity Density vs. Temperature.

The error bars are the standard deviations from the cavity size distributions, i.e., statistical error only.

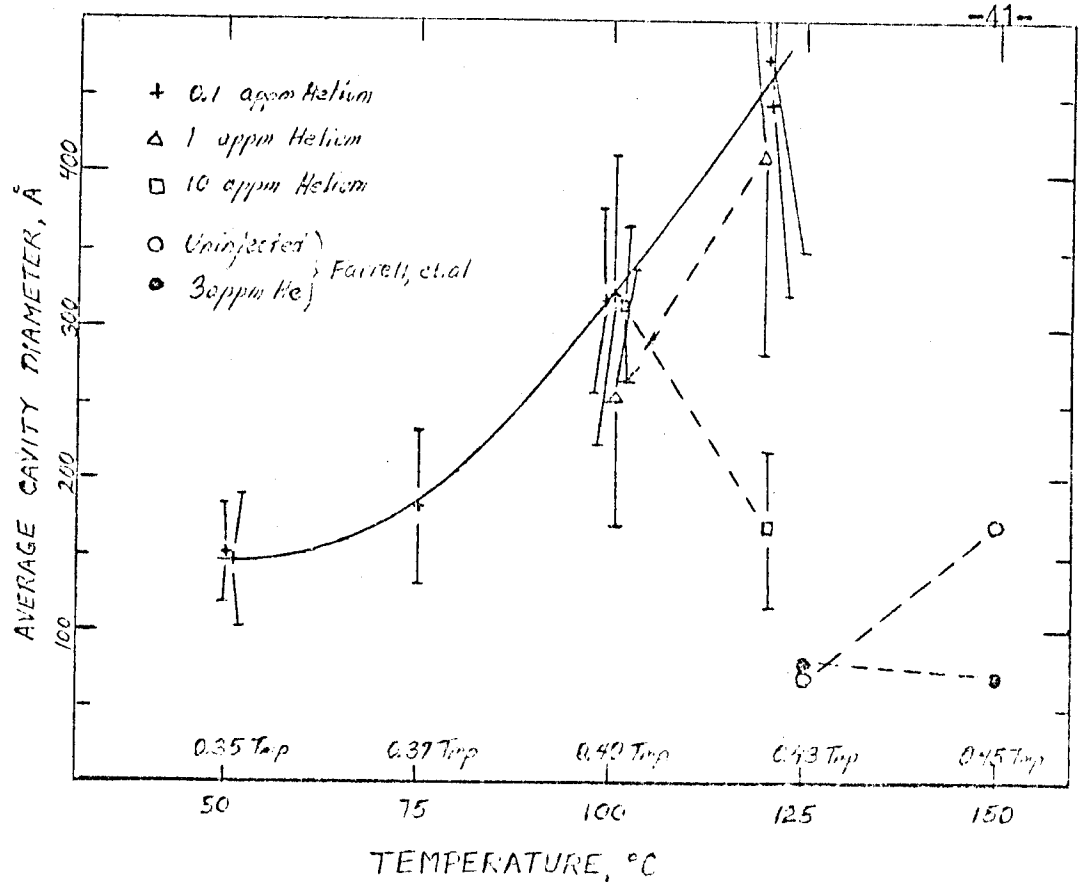
+ 0.1 appm Helium
△ 1 appm Helium
□ 10 appm Helium
○ Uninjected
● 3appm He
} Farrell, et.al
AVERAGE CAVITY DIAMETER, Å
100
200
300
400
0.35 Tmp
0.37 Tmp
0.40 Tmp
0.43 Tmp
0.45 Tmp
50
75
100
125
150
TEMPERATURE, °C

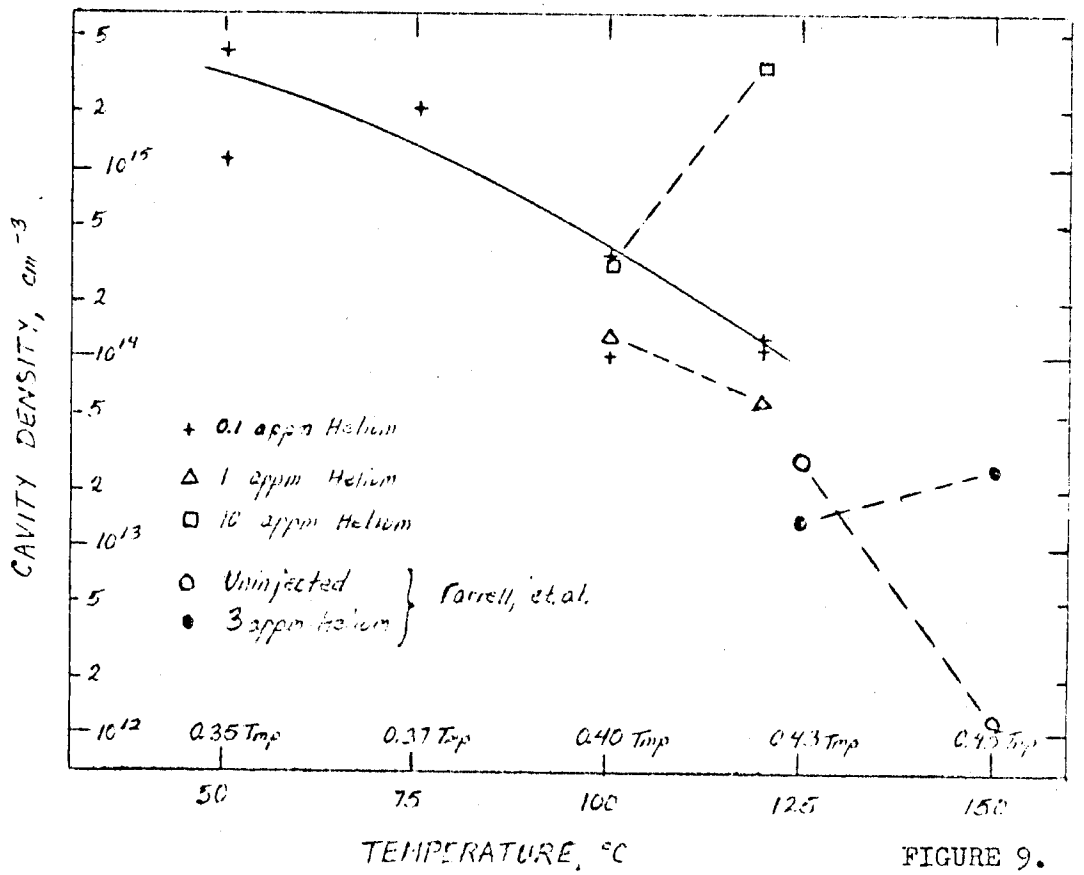
CAVITY DENSITY, cm⁻³
5
2
10¹⁵
5
2
10¹⁴
5
2
10¹³
5
2
10¹²
+ 0.1 appm Helium
△ 1 appm Helium
□ 10 appm Helium
○ Uninjected
● 3appm helium
} Farrell, et.al.
0.35 Tmp
0.37 Tmp
0.40 Tmp
0.43 Tmp
0.45 Tmp
50
75
100
125
150
TEMPERATURE, °C

FIGURE 9.

D. Variation with Helium Content

Since cavities did not form below 100°C in the 1 and 10 appm samples, the variation with helium content is only visible at 100°C and 120°C. At the lower of these temperatures there is no significant variation in cavity size or density (figure 10). The sample at 1 appm and 100°C has somewhat smaller cavities, but the statistical error alone easily accounts for this. At 120°C the cavity size decreased with increased helium and the density increased. This again matches the performance of the neutron-irradiated aluminum of Farrell, Wolfenden and King (1971), as seen in Table IV.

TABLE IV.

	125°C (Farrell, et al.)		150°C	
Uninjected	2.8×10^{13}	70 Å	1.2×10^{12}	170 Å
3 appm H	2.1 no	70 Å	6.7×10^{12}	100 Å
9 appm H	2.2 change	80 Å	1.5×10^{13}	80 Å
3 appm He	2.4	80 Å	2.6×10^{13}	70 Å
	100°C (This thesis)		120°C	
0.1 appm He	3.5×10^{14}	320 Å	1.1×10^{14}	460 Å
1 appm He	1.3 no	260 Å	6×10^{13}	410 Å
10 appm He	3.3 change	320 Å	3.4×10^{15}	170 Å

At the high temperature used in either study the cavity size decreases sharply as gas content rises. This trend continues in the 100 appm sample of Mazey, et al. (1973), but there are too many differences in this sample to weigh it more than qualitatively.

Both sets of data in Table IV also show a large increase in cavity

density with gas content, and Mazey's sample again follows this trend.

There are two growth models supported by these data. The behavior at the higher temperature in each experiment supports the homogeneous model, in agreement with the "normal" results at the 0.1 appm helium level discussed earlier. The increase in gas content allows more proto-clusters to survive and grow into cavities, and as the vacancies produced by the displacements are shared by these clusters, a higher density means fewer cavities per cluster, and thus a smaller average size.

At the lower temperature the variation in gas content does not seem to change the cavity size or density, lending support to a model of "displacement spike" nucleation. A spike can occur near the end of the path of an ion moving through the lattice. As the ion mean free path approaches the lattice spacing, all of the remaining energy of the ion will be deposited in a small region, producing a number of displacements and temporarily leaving a core rich in vacancies (Kelly, 1966 and Packan, 1971). According to the spike nucleation model, if several spikes occur close together in space and time, they may be able to form large cluster of vacancies which will not collapse, but will grow even without gas nucleation (Beeler,Jr., 1969). The fact that no cavities formed in the unimplanted aluminum casts some doubt on the complete independence from gas atoms, but if these spike-produced clusters could be stabilized equally well by small or large amounts of gas, then the resultant cavity density would depend only on the probility of simultaneous spikes. This probability depends only on the dose and the dose rate, and therefore the results at the lower temperatures in Table IV support this model.

It is possible that at the higher temperature the increased diffusion rates would prevent the aggregation of spikes which may occur at the lower

FIGURE 10. Average Cavity Diameter vs. Helium Content and Cavity Density vs. Helium Content at 100°C and 120°C.

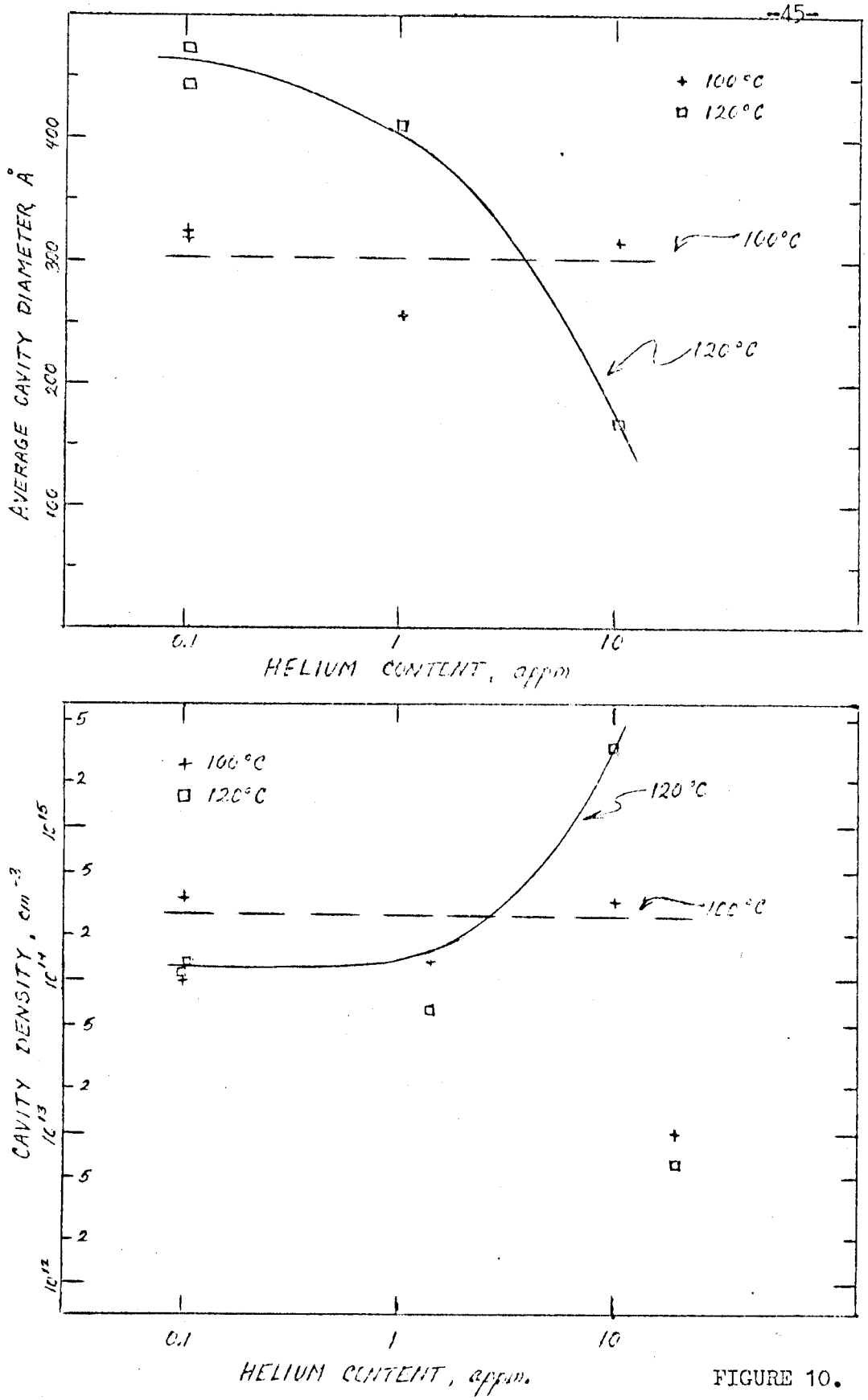
+ 100°C
□ 120°C
AVERAGE CAVITY DIAMETER, Å
400
300
200
100
100°C
120°C
0.1
1
10
HELIUM CONTENT, appm
+ 100°C
□ 120°C
CAVITY DENSITY, cm⁻³
5
2
10¹⁵
10¹⁴
10¹³
10¹²
120°C
100°C
0.1
1
10
HELIUM CONTENT, appm.

FIGURE 10.

temperature. A combination of the two mechanisms may be possible, with spike nucleation dominating at the lower temperature, and homogeneous nucleation dominating at the higher temperatures.

E. Variation in Swelling

The swelling depends on the cube of the cavity size and the first power of the density, and the combination of the large statistical errors makes it difficult to draw any conclusions from the swelling results.

TABLE V. Swelling

	50°C	75°C	100°C	120°C
0.1 appm He	0.2%, 0.6%	0.6%	0.6%, (0.2%)	0.6%, (0.6%)
1 appm He			(0.1%)	(0.2%)
10 appm He			0.6%	(0.8%)

The values in parentheses are from samples whose thicknesses were estimated; the other values were derived from the stereo thickness measurements described earlier.

F. Error Analysis

It is convenient to divide the error discussion into two parts: irradiation errors and measurement errors.

The measurement errors begin with the statistical variations in density and cavity size resulting from the sometimes small population counted. These probable errors were discussed earlier and are displayed

as error bars on the size curves (figures 9 and 10). The accuracy of the Zeiss Particle Size Counter determines the accuracy of the size measurement, and both size and density measurements depend on the accuracy of the magnification in the electron microscope and in the enlarging process. As claimed before, the statistical variations should overwhelm these mechanical errors. The density measurements also depend on the tilt accuracy of the specimen stage, the amount of material above and below the highest and lowest cavities, and above all on the assumption of thickness uniformity.

For the stereo photographs the $\pm 5^{\circ}$ angle was measured on the readout scale of a $\pm 30^{\circ}$ tilting stage. It is not improbable for this stage to be as much as $\pm 1^{\circ}$ off at a given setting, for a total error of $\pm 20\%$. A samples were observed in the same stage and specimen holder, however, so there should only be a small difference in angle change between samples. Improvements in angle measurement are not worth the added complexity until the foil thicknesses are uniform and cavity densities are high enough to reduce statistical variations.

There are three factors affecting the cavity size and density measurements: temperature, helium content and dose (dpa). Impurities other than helium can also play a part, but they should be constant and small throughout the experiment. The same is true for dose rate; its effect was ignored because it was fairly constant throughout the irradiations.

The temperature was measurable to within $\pm 2^{\circ}C$ and could be held within $\pm 3^{\circ}C$ of the nominal irradiation temperatures. Occasional variations up to $\pm 5^{\circ}C$ occurred, but more than 90% of the time on each irradiation was spent within $\pm 3^{\circ}C$ of the nominal temperature.

The helium levels depend on the dose and energy measurements, and on range and straggling values obtained from the literature. The actual helium contents may systematically differ from the nominal value, but the variation between samples of a particular level and the ratio of the 0.1, 1 and 10 appm levels should be within $\pm$10%, as the current and energy measurements are this accurate.

The dpa level depends on the accuracies of the current measuring system, the aluminum-ion beam energy, the depth of the prethinning, and ultimately, on the accuracy of the Mueller-Manning calculation. These dpa calculations are a standard means of comparison for different experiments; their validity must be determined within a framework broader than the results of one type of irradiation over a small energy range in one material. The accuracy of the current meter and integration method is better than $\pm$5%. The effect of secondary electrons, which in positive-ion bombardment makes the beam current appear larger, has been roughly measured by the use of secondary-suppressing biasing. It causes about a 100% increase in measured beam current, and although this may seem to be a large error, it is constant for all the samples in the experiment. If necessary for comparison with other data the dpa levels reached here may be reduced by 50%, but this will not affect any of the important results of this thesis.

The ion beam energy is measured by an alternating current voltmeter connected to a set of rotating vanes in the electric field of the accelerator high-voltage terminal. As this system has been calibrated repeatedly over many years with many nuclear reaction thresholds, its calibration is known to within about 2%. Including error in the voltmeter and allowed variation during irradiations, the energy should be accurate to

within ±5%.

Finally, the assumption of the uniformity of the prethinning step can be assessed, as depth of prethinning has a strong bearing on the dpa values. The uniformity of removal from one end of a sample strip to the other is demonstrated by reasonable differences in observed cavity sizes for those samples irradiated on the same strips, shown in Table VI.

TABLE VI

A-0-X1-23	100°C	320 A ±55 A
A-0-X1-24	0.1 appm	320 A ±100 A
A-0-X1-42	120°C	450 A ±130 A
A-0-X1-43	0.1 appm	470 A ±130 A
A-0-X1-46	50°C	140 A ±45 A
A-0-X1-47	0.1 appm	150 A ±30 A

The difference in cavity size between samples irradiated under the same conditions is well within the possible random deviation; this not only implies uniformity in the prethinning technique, but it reflects the repeatability and precision of the entire experimental procedure from the helium implanting through the irradiation to the prethinning and preparation for electron microscopy.

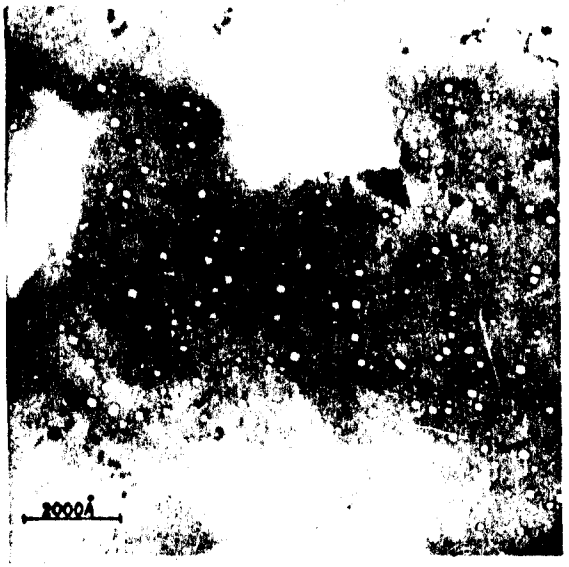

50°C
A-0-XI-46

75°C
A-0-XI-45

100°C
A-0-XI-23

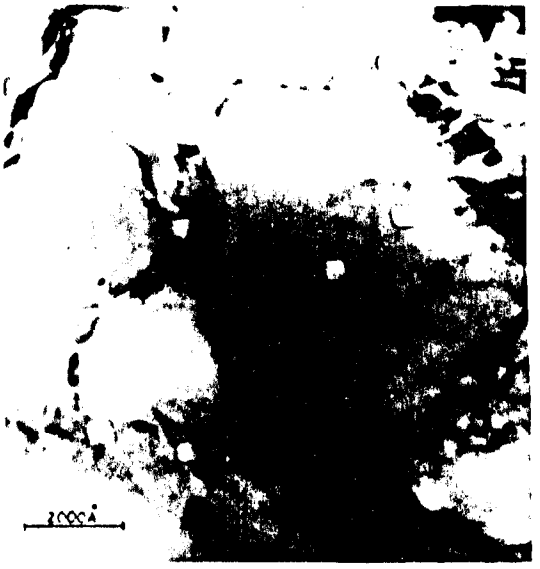

120°C
A-0-XI-22

Effect of temperature on crystal size and density at 0.1 atom fraction

FIGURE 11

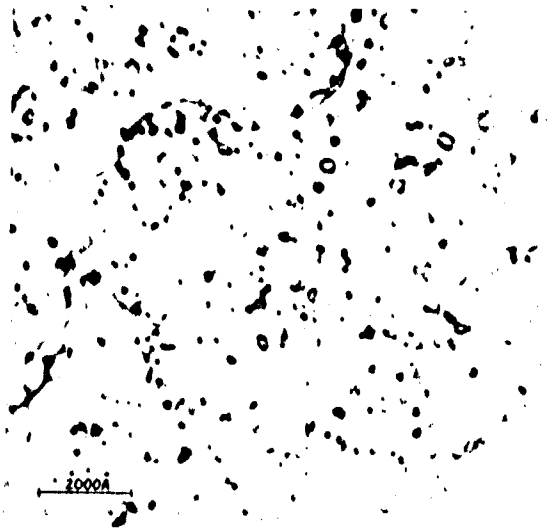

50°C
A-0-01-32

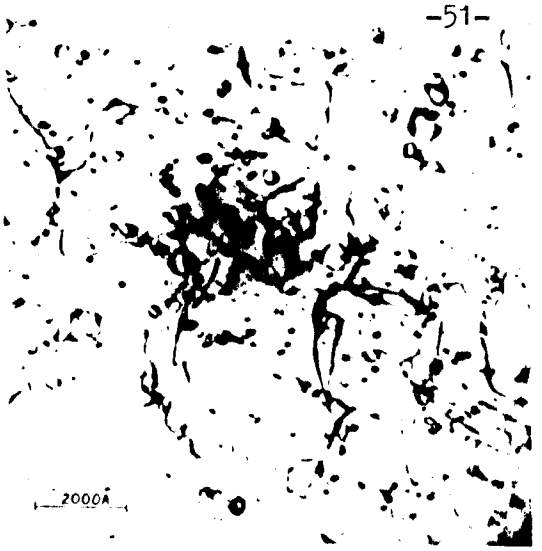

75°C
A-0-01-30

100°C
A-0-01-26

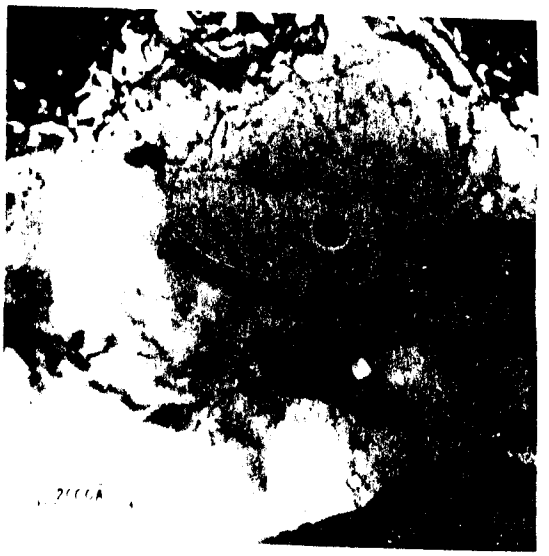

120°C
A-0-01-27

Effect of temperature on loop and cavity size and density at 1 appm Helium.

FIGURE 12

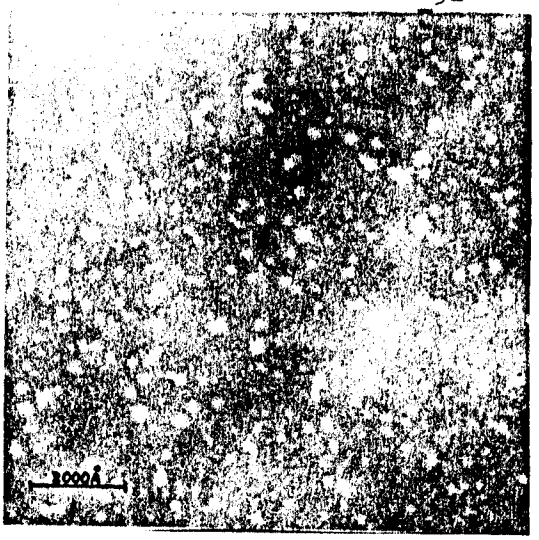

120°C 1.9dpa
A-0-10-20

100°C 1.9dpa
A-0-10-18

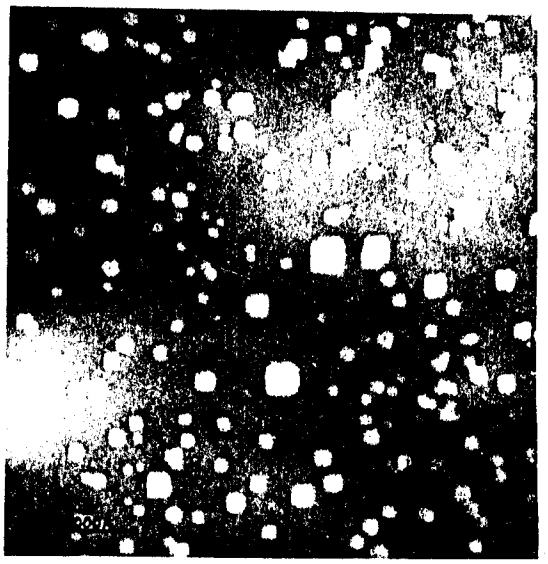

120°C 4.3dpa
A-0-10-22

Effect of temperature and dose on cavity size and density at 10 appm Helium

FIGURE 13

No Helium
A-0-00-8

0.1 appm Helium
A-0-X1-23

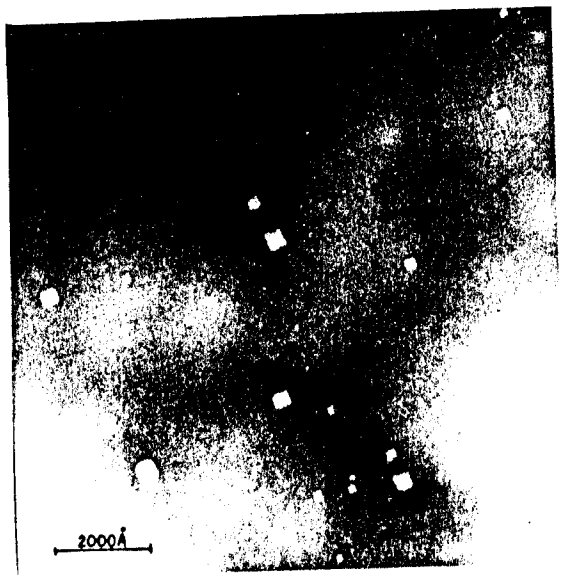

1 appm Helium
A-0-01-26

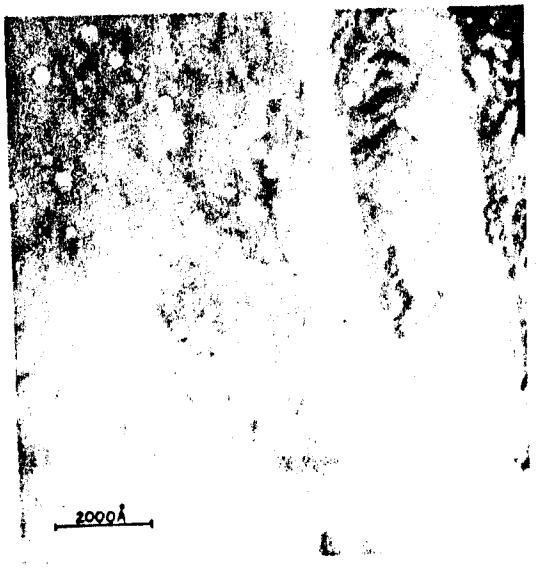

10 appm Helium
A-0-10-18

Effect of Helium content on cavity size and density at 700°C.

FIGURE 14

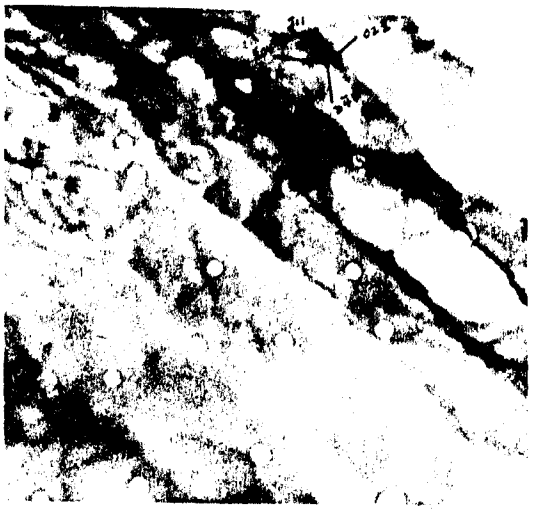

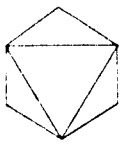

(111)
A-O-10-18
126,000x

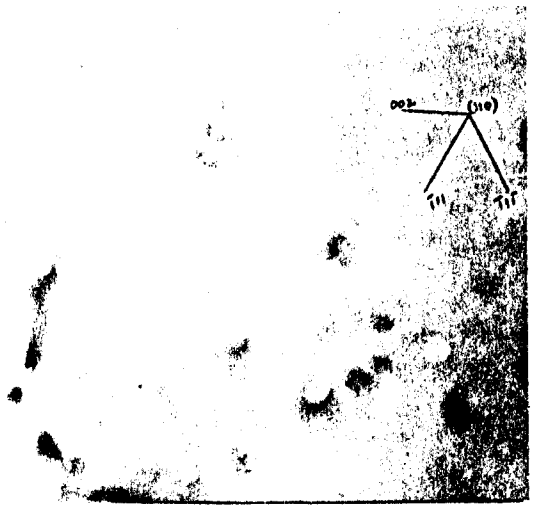

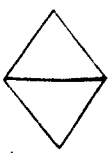

(110)
A-O-XI-46
320,000x

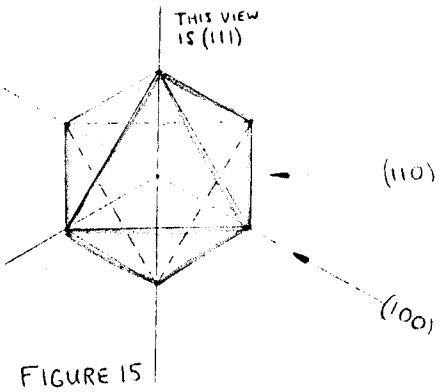

FIGURE 15
CAVITY SHAPE AND ORIENTATION

VI. Conclusion

There are two basic results of this thesis: that a nucleating gas is required for the production of cavities in a pure material and that self-ion bombardment can duplicate the same kind of variations in cavity formation with variations in temperature and gas content that are produced in fast-neutron irradiation.

The complicated procedure developed for this project has produced results which when seemingly not self-consistent, i.e., reversal of cavity size and density slopes at 10 appm helium, were consistent with the behavior of the same material in fast-neutron irradiation. The precision of the measurement techniques and the irradiation controls are reflected in the reproducibility of those samples which existed in duplicate.

Future work should extend the temperature range in the pure material to confirm the need for a nucleating gas at higher temperatures and at higher doses. Helium-implanted samples should also be irradiated over a wider temperature range, and the cavity-formation threshold should be measured at the lower temperatures at 1 and 10 appm helium. It is important to obtain a complete temperature variation curve at 10 appm helium, probably at higher doses, and to confirm the "reversed" cavity size and density at the doses in this experiment.

VII. Appendices

A. Table of impurities found in the Cominco lot HPM 7767 high-purity aluminum, in appm (Packan, 1971)

B	1.0
Ca	0.6
Cr	0.08
Cu	0.06
Fe	0.3
In	0.04
K	0.5
Mg	0.3
Mn	0.04
Na	0.1
Ni	0.07
Si	4.
Ta	0.04
Ti	0.1
Zn	0.4
Total	7.3

Appendix B. Displacement-Density Calculations for Aluminum Ions on an Aluminum Target

The basic displacement calculation uses the stopping-power theory of Lindhart, Scharff and Schiøtt (1963) which provides the electronic and nuclear stopping powers, $(dE/dx)_e$ and $(dE/dx)_n$, as a function of the path length of an ion of energy E_1, mass m_1, and atomic number z_1, incident on a target of mass m_2 and atomic number z_2. The stopping powers are expressed in terms of dimensionless energy and range terms, ε and ρ, where

$$\varepsilon = \frac{E}{E_L} \quad \text{and} \quad \rho = \frac{R}{R_L} \tag{B1}$$

where

$$E_L = Z_1 Z_2 e^2 \ (m_1 + m_2)/ \ am_2 \tag{B2}$$

and

$$R_L = (m_1 + m_2)^2/ \ 4\pi a^2 N m_1 m_2 \tag{B3}$$

where the screening length a is

$$a = 0.8853 \ (\hbar^2/mc^2)(Z_1^{2/3} + Z_2^{2/3})^{-\frac{1}{2}} \tag{B4}$$

Here, m and e are the mass and charge of the electron and R is the path length of the incident ion.

Combining the LSS nuclear stopping power term with the cosine of the average scattering, $\langle \cos \Phi \rangle$, the nuclear energy loss per unit depth can be calculated:

$$\left(\frac{d\mathcal{E}}{d\rho_d}\right)_n = \frac{1}{\langle \cos\varphi \rangle}\left(\frac{d\mathcal{E}}{d\rho}\right)_n \qquad (B5)$$

where ρ_d is now the dimensionless penetration depth, rather than the total path length.

The energy is given to recoil atoms along the cascade, but these atoms suffer additional electronic energy losses, indicating that a reduced amount of energy is all that is available for displacement production. Thus reduced damage energy, $\mathcal{E}_D$, can be obtained from the damage efficiency term of Lindhard, Nielson, Scharff and Thomsen (1963),

$$\omega_D(\mathcal{E}) = \frac{1}{1 + kg(\mathcal{E})} \quad , \quad \mathcal{E}_D = \omega_D \mathcal{E} \qquad (B6)$$

where k is an LSS constant,

$$k = 0.133745 \frac{Z^{2/3}}{A^{1/2}} \qquad (B7)$$

and $g(\mathcal{E})$ is an LSS parameter approximated by Robinson (1972) as

$$g(\mathcal{E}) = 3.4008\,\mathcal{E}^{1/6} + 0.40244\,\mathcal{E}^{3/4} + \mathcal{E} \qquad (B8)$$

Using this damage efficiency term, the damage energy per unit depth is

$$\frac{d\mathcal{E}_D}{d\rho_d} = \frac{1}{\langle \cos\varphi \rangle} \int_0^{\mathcal{E}} \omega_D(x)\, f(x)\, dx/\mathcal{E} \qquad (B9)$$

where $f(x)$ is the LSS universal function of ion masses and energies.

The displacement density at any depth in displacements per atom of target (dpa) is

$$\text{dpa} = (J/N)(E_L/R_L)(\beta/2E_d)(d\mathcal{E}_D/d\rho_d) \qquad (B10)$$

where J is incident current, ions/cm^2, N is the target atomic density, β is an efficiency factor, and E_d is the energy required to displace a

target atom.

The Mueller-Manning calculation follows this basic outline with additional corrections for straggling, especially important near the particle paths. The calculation results for 1.2 and 1.4 Mev aluminum ions on an aluminum target (figures B-1 and B-2) are for a dose of 10^{16} ions/cm^2; they were reduced linearly to match the actual sample doses in Table I.

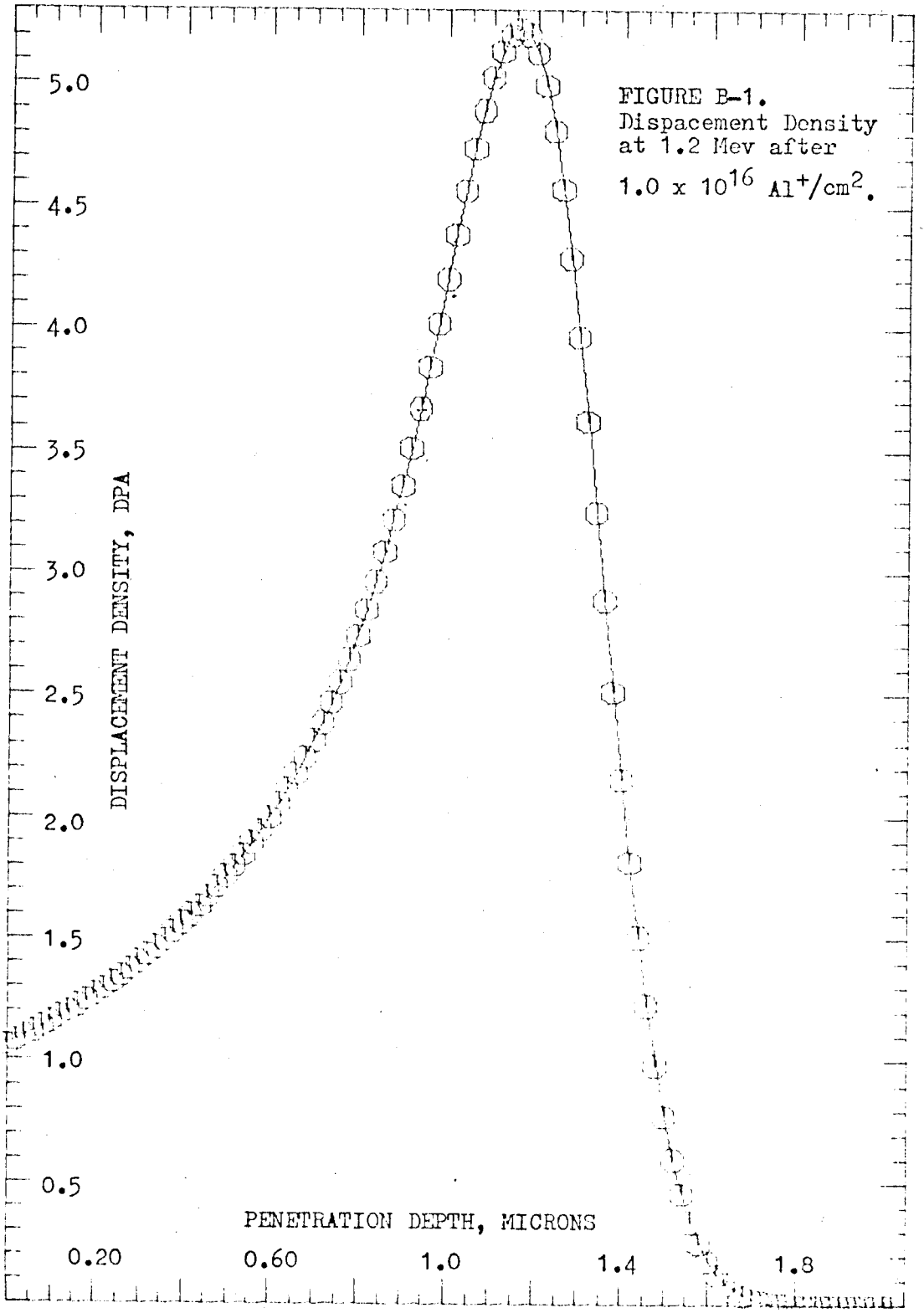

FIGURE B-1.
Dispacement Density at 1.2 Mev after 1.0×10^{16} Al^{+}/cm^{2}.

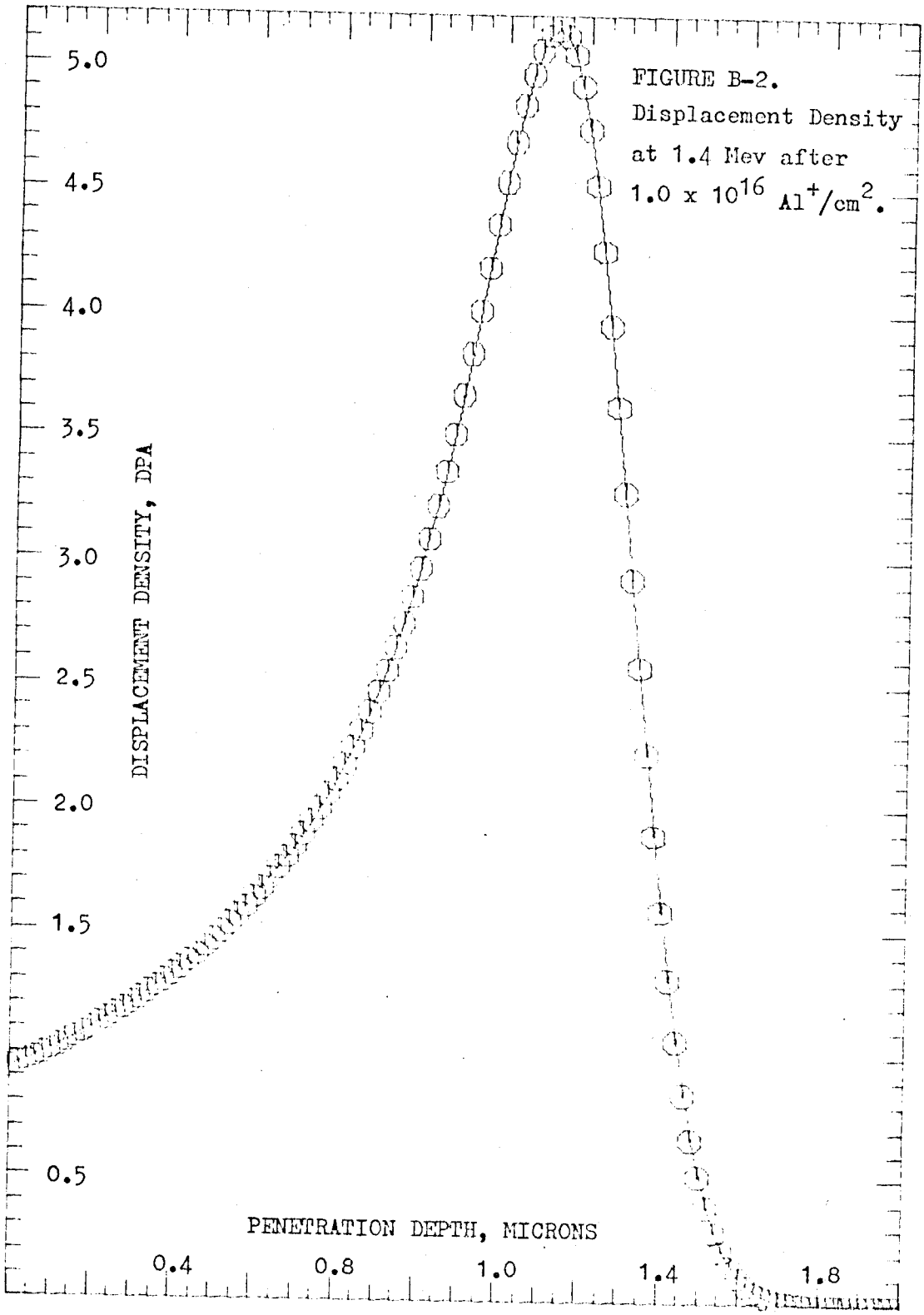

FIGURE B-2.
Displacement Density at 1.4 Mev after 1.0×10^{16} Al^{+}/cm^{2}.

Appendix C. Table of Irradiation Data for Samples Containing only Dislocation Loops.

Sample	E	Al^{+}/cm^{2}	Time	Temp	Depth*	DPA	DPA/sec
A-0-00-8	1.2	5.5×10^{15}	71	100	A/S .77	1.45	3.4×10^{-4}
A-0-0010	1.5	5.3	86	100	A/S .85	1.10	2.1
A-0-00-11	1.5	5.3	114	75	A/S .80	1.02	1.5
A-0-00-12	1.5	5.3	81	75	A/S .80	1.02	2.1
A-0-00-13	1.45	5.3	110	120	A/S .85	1.06	1.6
A-0-00-14	1.45	5.3	102	120	A/S .85	1.06	1.7
A-0-00-15	1.5	5.3	118	50	A/S 1.14	1.83	2.6
A-0-00-16	1.45	5.3	118	50	A/S 1.14	1.83	2.6
A-0-00-17	1.35	2.3×10^{16}	400	100	A/S 1.24	11.0	4.6
A-0-01-30	1.4	5.3×10^{15}	110	75	C 1.17	2.25	3.4
A-0-01-31	1.4	5.3	102	50	C 1.17	2.25	3.7
A-0-01-32	1.4	5.3	105	50	C 1.17	2.25	3.6
A-0-10-36	1.2	5.3	146	75	C 1.02	2.30	2.6
A-0-01-37	1.2	5.3	88	75	C 1.01	2.28	4.3
A-0-01-39	1.2	5.3	134	50	C 1.08	2.59	3.2
A-0-01-40	1.2	5.3	105	28	C 1.08	2.59	4.1
A-0-01-41	1.2	5.3	96	30	C 1.08	2.59	4.5
	Mev	(Dose)	Min.	°C	Microns		

*A/S means that the prethinning was done by anodizing/oxide stripping.

C means that a chemical polish was used to prethin the sample.

Bibliography

1. R.S. Barnes and D.J. Mazey, Phil. Mag., 5 (1960) 1247.

2. R.S. Barnes and D.J. Mazey, Proc. R. Soc., A275 (1963) 47.

3. J.R. Beeler, Jr., in reference 50 (1962)

4. A.E. Blaugrund, Nuc.Phys., 88 (1966) 501.

5. H.R. Brager, H.E. Kissinger, G.L. Kulcinsli, BNWL-SA-3374 (1970).

6. J.L. Brimhall and B. Mastel, J. Nuc. Mat., 19 (1969) 123.

7. J.L. Brimhall and B. Mastel, Proceedings 27th EMSA Meeting (1970) 186.

8. J.A. Brinkman, J. Appl. Phys., 25 (1954) 961.

9. R.A. Brinkman, Radiation Damage nei Solidi, Societa Italian Di Fisica, XVIII Corso, Academic Press (1962)

10. R. Bullough and R.C. Perrin, in reference 50 (1969) 233.

11. R. Bullough and R.C. Perrin, in reference 49 (1972) 769.

12. R. Bullough and R.C. Perrin, Proc. R. Soc., A305 (1968) 541.

13. T.T. Claudson, J.J. Holmes, J.L. Straalsund, H.R. Brager, in reference 50 (1969).

14. K. Farrell, J.T. Housten, A. Wolfenden, R.T. King and A. Jostsons, in reference 49 (1972) 380.

15. K. Farrell, A. Wolfenden and R.T. King, Rad. Effects, 8 (1971) 107.

16. S.D. Harkness, Che-yu Li, in Reference 50 (1969) 189.

17. S.D. Harkness and Che-yu Li, Met. Trans., 2 (1971) 1457.

18. A. Jostsons, E.L. Long, Jr., J.O. Stiegler, K. Farrell and D.N. Braski, in reference 49 (1972) 363.

19. D.W. Keefer, H,H, Neely, J.C. Robinson, A.C. Pard, D. Kramer, "Void Formation in Proton-Irradiated Stainless Steel", AEC Contract AT(04-3)-701 (1970).

20. D.W. Keefer and A.G. Pard, J. Nuc. Mat., 47 (1973) 97.

21. B.T. Kelly, Irradiation Damage to Solids, Pergammon Press (Oxford, 1966).

22. G.H. Kinchin and R.S. Pease, Reports Prog. Phys., 18 (1955) 1.

23. G.L.Kulcinski, D.G. Doran and J.J. Laidler, Rad. Effects, 7 (1970) 195.

24. P. Linhagen, in reference 50 (1969) 401

25. J. Lindhard, M. Scharf and H.E. Schiøtt, Mat. Fys. Medd. Dan. Vid. Selsk., 33 (1963) 14.

26. J. Lindhard, V. Nielson, M. Scharf, P.V. Thomsen, Mat. Fys. Medd. Dan. Vid. Selsk., 33 (1963) 10.

27. E.S. Mashkova and V.A. Molchanov, Rad. Effects, 16 (1972) 143.

28. I. Manning and G.P. Mueller, Computer Phys. Communication, 6 (1973) 1.

29. D.J. Mazey and R.S. Barnes, Phil. Mag., 7 (1962) 1861.

30. D.J. Mazey and R.S. Barnes, Phil. Mag., 17 (1968) 387.

31. D.J. Mazey, S. Francis and J.A. Hudson, J. Nuc. Mat., 47 (1973) 137.

32. K.L. Merkle, BNL 50083, BNL (1967) 359.

33. R.S. Nelson, D.J. Mazey and R.S. Barnes, Phil. Mag., 11 (1965) 91.

34. R.S. Nelson and D.J. Mazey, in reference 50 (1969) 157.

35. L.C. Northcliffe and R.F. Schilling, Nuc. Data, 1, 3-4 (1970) 233.

36. O.S. Oen and M.T. Robinson, Appl. Phys. Letters, 2 (1963) 83.

37. N.H. Packan, Thesis, ORNL-TM-3109 (1971).

38. N.H. Packan, J. Nuc. Mat., 40 (1971) 1.

39. M.T. Robinson, in reference 49 (1972) 397.

40. A. Seeger, in reference 50 (1969) 50.

41. P.G. Shewmon, Science, 173 (1971) 987.

42. G. Sidenius and O. Skilbreid, E.M. Separation of Radioactive Isotopes, Proc. International Symp., Vienna, May 1960, Springer-Verlag (Wien, 1961).

43. J.O. Stiegler, K. Farrell, C.K.H. Dubose and R.T. King, in reference 50 (1969) 215.

44. M.W. Thompson, Defects and Radiation Damage in Materials, Cambridge Univ. Press (Cambridge, 1969).

45. M.W. Thompson and S.B. Wright, J. Nuc. Mat., 16 (1965) 146.

46. K.H. Westmacott and R.E. Smallman, Mat. Sci. Eng., 5 (1969/70) 325.

48. Proceedings of the BNES European Conference, Voids Formed by Irradiation of Reactor Materials, ed. by S.F. Pugh, N.H. Loretto and D.I.R. Norris, Reading, U.K., March 1971 (1971).

49. Proceedings of the International Conference, Radiation-Induced Voids in Metals, ed. by J.W. Corbett and L.C. Ianniello, Albany. N.Y., June 1971, AEC Symposium Series, CONF-710601 (1972).

50. Proceedings of the IAEA Symposium, Radiation Damage in Reactor Materials, Vienna, June 1969, STI-PUB-230 (1969).